ENHANCING WAVELENGTH SENSING RANGE OF SPR-PCF USING DUAL PEAK DOUBLE RESONANCE: AN LSPR BASED APPROACH

by

Wasifa Rahman Rashmi, 180021218
Maisha Farjana Etu, 180021222
Sarah Abbas, 180021225

A Thesis Submitted to the Academic Faculty in Partial Fulfillment of the requirements for the Degree of

BACHELOR OF SCIENCE IN ELECTRICAL AND ELECTRONIC ENGINEERING

Department of Electrical and Electronic Engineering,

Islamic University of Technology (IUT),

Gazipur, Bangladesh.

May 2023

ENHANCING WAVELENGTH SENSING RANGE OF SPR-PCF USING DUAL PEAK DOUBLE RESONANCE: AN LSPR BASED APPROACH

Approved By:

Prof. Dr. Mohammad Rakibul Islam

Supervisor and Professor,
Department of Electrical and Electronic Engineering,
Islamic University of Technology (IUT)
Board bazar, Gazipur- 1704

Date: 26-05-23

DECLARATION OF AUTHORSHIP

We, Wasifa Rahman Rashmi (180021218), Maisha Farjana Etu (180021222), and Sarah Abbas (180021225), hereby declare that the thesis titled "ENHANCING THE WAVELENGTH SENSING RANGE OF SPR-PCF USING DUAL PEAK DOUBLE RESONANCE: AN LSPR-BASED APPROACH" and all the information contained therein are the results of our individual efforts and original contributions.

We confirm that:

- This work has been completed in partial fulfillment of the prerequisites for the Bachelor of Science in Electrical and Electronic Engineering degree at Islamic University of Technology.
- The contents of this thesis have never before been submitted to a university in order to earn another degree.
- When consulting published work by others, we consistently provide due credit to the sources.

Signatures of Students:

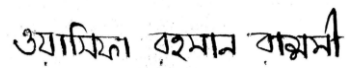

Wasifa Rahman Rashmi
Student ID: 180021218

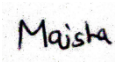

Maisha Farjana Etu
Student ID: 180021222

Sarah Abbas
Student ID: 180021225

Table of Contents

ACKNOWLEDGEMENTS

Praise to Almighty Allah (SWT), who has given us the perseverance, patience and fortitude to complete our thesis as a prerequisite for partial fulfilment for the Bachelor of Science in Electrical and Electronic Engineering degree. We extend our cordial gratitude to our honourable thesis supervisor Prof. Dr. Mohammad Rakibul Islam, Department of Electrical and Electronic Engineering, Islamic University of Technology for his constant support, unwavering patience and nurturing guidance. Without his outstanding guidance and knowledge during the ideation and research phases, the thesis would not have been as effective. We would like to express our appreciation to the Electrical and Electronic Engineering faculty for their insightful comments, helpful advice, and constructive criticism provided throughout the pre-defence and defense, all of which enabled us to enhance our study. Finally, we would like to express our gratitude to the entire team for their numerous contributions to this project. Each team member made a big contribution to its success, and we are tremendously grateful for their dedication and labour of love. Finally, we would like to sincerely thank everyone who made a substantial contribution to our thesis.

ABSTRACT

A novel sensor developed using GZO and gold as plasmonic materials is proposed in this work. We have designed our sensor in COMSOL Multiphysics software v5.6 and performed its numerical investigation utilizing the FEM. The simulation results manifested the fact that double resonance peaks were created at two specific wavelengths due to the exclusive dispersion relation arising by the concurrent use of two plasmonic materials. A unique parameter termed as DPSS has been presented by taking shifting of the double resonance peaks into consideration and the optimization of the presented design has been accomplished with a view to achieving the maximum value of DPSS. At optimal design conditions, a highest DPSS value of 11,720 um/ RIU was acquired, and the sensor depicted the potentiality of analyte detection constituting a wide RI range of 1.30 to 1.40. Furthermore, the working range of the sensor was found to be in the broad wavelength spectrum of 0.3 um to 0.98 um which ascertains its efficacy in both the ultra-violet and visible spectral range. An acutely low value of Confinement Loss (CL) has also been illustrated by the sensor making it appropriate for larger sensor lengths[1]. Moreover, the sensor we proposed demonstrated a maximal Wavelength Sensitivity (WS) of 11,480 nm/RIU while detecting analytes constituting the range of RI of 1.39-1.40 with a precise sensor resolution value of 8.71×10^{-6} RIU correspondingly. Therefore, expediency of the sensor in both the ultra-violet and visible spectrum range confirms its novelty and credibility in a diverse range of biosensing applications while its high DPSS and WS values, minute wavelength resolution value and low CL values uphold its position as an efficacious medium of analyte detection in the field of biosensing.

List of Figures

List of Tables

List of Abbreviations

AS: Amplitude Sensitivity

CL: Confinement Loss

CLR: Confinement Loss Ratio

CT: Crosstalk

EMF: Electromagnetic Field

EML: Effective Material Loss

ER: Extinction Ratio

FEM: Finite Element Method

FOM: Figure of Merit

LSPR: Localized Surface Plasmon Resonance

NA: Numerical Aperture

NIR: Near-infrared Region

PCF: Photonic Crystal Fiber

PML: Perfectly Matched Layer

RI: Refractive Index

RIU: Refractive Index Unit

SP: Surface Plasmon

SPP: Surface Plasmon Polariton

SPR: Surface Plasmon Resonance

SPW: Surface Plasmon Wave

TE: Transverse Electric

THz: Terahertz

TIR: Total Internal Reflection

TM: Transverse Magnetic

WS: Wavelength Sensitivity

GZO: Gallium doped Zinc Oxide

RS: Relative Sensitivity

CHAPTER 1

INTRODUCTION

1.1 Background

A biosensor is a sophisticated medium that detects biological or chemical reactions by creating signals that are proportional to the concentration of an analyte participating in the reaction[2]. Biosensors can be used for a wide range of applications, including but not limited to disease monitoring, drug discovery, and disease indicators in bodily fluids. Three fundamental components make up a biosensor: signal generator based on the target analyte, a transducer and a reading device that records and decodes the created signal[3]. The first recorded use of biosensors was found to be in the 1960s by pioneers Clark and Lyons[4]. Different types of biosensors comprise enzyme-based sensors, tissue-based sensors, thermal and piezoelectric biosensors, as well as other types of sensors.

Optical biosensors leverages the interaction between light and the target analyte to differentiate between different substances [5]. Because of their multiple advantages, optical biosensors have received substantial interest and widespread implementation. These cutting-edge sensors enable the detection of a wide range of biological and chemical compounds in real time and without the need of labels. Owing to the high specificity and sensitivity, optical sensors are knows to provide high accuracy. Furthermore, their small size and low cost make them ideal for a variety of applications[6]–[9]. The capacity of optical biosensors to detect without the need for extensive pre-treatment operations, keeping the integrity and nature of the target molecules, is one prominent feature. This feature not only streamlines the whole study technique, but it also reduces the possibility of changing the properties of the substances being researched[6]. Furthermore, optical biosensors have a significant potential for integration into a single chip, allowing for the creation of compact and highly functional sensor arrays [5], [6], [8].

The term "label-free detection" describes a method used by optics-based biosensors to measure the changes that take place when an analyte binds to a ligand immobilized on the surface of the biosensor[10]. Without the use of artificial manipulation or the inclusion of extra labels or markers, this technique enables real-time observation of the interaction. Label-free detection provides a direct and pure way to track binding events by taking advantage of the unique characteristics of the analyte-ligand interaction, enabling more precise and dynamic analysis in biosensing applications. The integrity of the biological system under investigation is preserved by avoiding the addition of exogenous labels that can change the behaviour or properties of the analytes.

Surface plasmon resonance (SPR), another label-free detection technique, uses optics-based biosensors to monitor changes in a thin metal layer's refractive index as a result of the binding of biomolecules to its surface[11]. With this method, biomolecular interactions can be directly observed in real time without the use of labelling chemicals. Without the use of fluorescent or other detection labels, surface plasmon resonance (SPR) offers real-time evaluation of molecular affinity, kinetics, specificity, and concentration of biomolecules[12]. By utilizing their size and binding characteristics, individual proteins, nanoparticles, virions, and exosomes can be imaged using surface plasmon resonance (SPR), which offers valuable, label-free information about their characteristics[13].

1.2 Problem statement

SPR based PCF sensors are optical biosensors that use the SPR phenomenon on a PCF substrate to detect changes in the refractive index of the surrounding medium. This cutting-edge sensing method makes it possible to monitor local environmental changes without the need of labels, providing a very sensitive and adaptable platform for biosensing applications[14]. Some generalized types of the SPR based PCF sensors:

1. Internal sensing: The metal coating and analyte solution dwell within the fiber in a unique arrangement used by internal sensing based SPR-based PCF sensors[15]. These sensors provide remarkable sensitivity and resolution by adopting a variety of PCF architectures, including D-shaped, U-shaped, circular, and elliptical designs. With this novel method, changes in the refractive index may be precisely and accurately detected, making it a very effective tool for a variety of biosensing applications. Internal sensing SPR-based PCF sensors require a complex and time-consuming liquid infiltration procedure, and their detecting range is limited by the limited length of the metal layer within the fiber[15].

2. External sensing: The coating of the metal is applied to the fiber's outside while an analyte solution encircles the fiber in the PCF-SPR sensor design[16]. The production and use of the sensors are simplified by this design because it does not require a liquid infiltration procedure[15]. Due to light leakage from the metal-coated surface, SPR-based PCF sensors display increased confinement loss compared to internal sensing sensors. As a result of the weaker interaction between the SPR field and the analyte in this configuration, they also have inferior resolution. Based on the unique needs of the application, these elements should be taken into account while choosing the best sensing platform.
3. Hybrid sensing: SPR-based hybrid sensing-based PCF sensors have a special arrangement where the metal coating is positioned both inside and outside the fiber[16]. This design makes it possible to merge the advantages of internal and external sensing techniques, improving sensor performance. These sensors may be able to lessen the drawbacks related to internal or external sensing alone by utilizing this hybrid technique. Due to the necessity of applying both internal and external metal coatings, SPR-based PCF sensors exhibit higher fabrication complexity than internal or external sensing sensors[15]. The production process is made even more complex and precise by the dual-coating technique.

1.3 Objective

An innovative method of sensing in the modern era is the investigation of SPR based PCF sensors. Additionally, there is still a lot of room for improvement in the wavelength sensing capabilities of SPR-based PCF sensors, especially in the ultraviolet (UV) spectrum. A fascinating and unexplored possibility for further research is the exploration of sensing capabilities in various wavelength ranges. In light of this, the adoption of SPR-based PCF sensors represents a cutting-edge and promising approach in sensing, giving intriguing opportunities for advancing technological and scientific applications in this area. So, the key objectives of this research can be summarized as:

1. Developing a unique design in surface plasmon resonance (SPR) sensors to attain a wider detecting range and higher sensitivity.
2. Optimization of various parameters to enhance sensor performance and increase sensitivity to minute changes in analyte properties, such as sensor structure, coating materials, or excitation techniques.
3. Exploring the implementation of simultaneous use of multiple plasmonic materials.
4. Increasing the RI detection range of the sensor.

5. Potential uses in environmental monitoring, healthcare, and other industries where advanced detecting capabilities are needed.

1.4 Motivation

The goal of this thesis is to address several issues with PCF-based SPR sensors, including their limitations and difficulties. Due to the narrow wavelength range revealed in earlier studies, these sensors can only be used in a limited range of wavelengths. Their adaptability and promise for wider sensing applications are hampered by this constraint. By removing this restriction, it is possible to investigate a greater variety of analytes and modify the sensors to meet various measurement needs.

The restricted wavelength sensitivity and resolution of SPR-based PCF sensors is a crucial issue that demands study. For reliable and exact detection, especially when analytes are present in low quantities, higher sensitivity and resolution are essential. The detection capabilities of SPR-based PCF sensors would be improved by addressing these issues, which would also make it possible to analyze analytes more precisely and reliably.

Additionally, earlier research has not fully utilized the simultaneous usage of two materials in SPR-based PCF sensors. This offers a chance to investigate how pairing materials with complementary features can improve sensing performance. It might be possible to enhance sensor sensitivity, selectivity, and overall performance by taking advantage of the distinctive properties of various materials.

The difficulty of fabricating SPR-based PCF sensors is another crucial issue that needs to be solved. In addition to lowering production costs, streamlining and simplifying the fabrication process would increase the accessibility of these sensors for researchers and business people. The general adoption and practical deployment of SPR-based PCF sensors can be considerably aided by the development of new manufacturing techniques or by improving currently used techniques.

The goal of this thesis is to offer novel SPR-based PCF sensor designs that overcome the constrained wavelength range, enhance wavelength sensitivity and resolution, investigate the simultaneous use of two materials, and optimize fabrication procedures by addressing these difficulties and constraints. The ultimate objective is to improve the functionality and adaptability of SPR-based PCF sensors, enabling their use in a variety of industries and sectors, such as biomedical research, environmental monitoring, and industrial analysis. The results of

this study should help biosensing technologies progress by delivering more precise, dependable, and effective tools for chemical and biological analyses.

1.5 Thesis Framework

The thesis book is constructed of the chapters as follows:

Chapter 2: This chapter gives a brief description of the contemporary works on PCF sensors used for Thz sensing, discusses on PCF waveguide, and finally the application of SPR with PCF.

Chapter 3: A detailed discussion on PCF, its working principle, and its applications are provided.

Chapter 4: The implementation of SPR along with PCF sensors is explored. The working principle is elaborately discussed. Its advantages and success rate that inspired us to work with SPR has been explained. The drawbacks of integrating SPR with PCF sensors have also been included. Besides, this chapter is focused on LSPR which is a unique application of SPR. The working principles of LSPR and its applications have been elaborately explained.

Chapter 5: Provides all the equations required for numerically solving the electromagnetic equations. It includes the optical equations of the materials including Drude-Lorentz equations of gold and GZO, Sellmier equation of silicon, confinement loss equation, equations of necessary performance parameters like WS, resolution etc., and a novel performance parameter DPSS's equation.

Chapter 6: The design and the theoretical modelling of the proposed SPR based PCF, optimization of the design parameters, dispersion characteristics, sensor calibration, diverse expansion of sensor length, sensor resolution, sensor linearity, double resonance, DPSS performance, and a comparison with previous works have been discussed here.

Chapter 7: The fabrication of the sensor has been proposed here. A discussion on stack and draw method and CVD technique have been included.

Chapter 8: This chapter includes the conclusion of the thesis book. Lastly an overview of the future aim has been provided.

CHAPTER 2

LITERATURE REVIEW

In the field of optical communication and bio-sensing, SPR based PCFs have proven to be immensely effective for myriad applications[17][18]. When a photon beam falls on the core of the PCF, the electromagnetic field reaches the region of the cladding in a partial manner due to which the surface electrons on the plasmonic materials get excited upon the interaction of the evanescent field with the plasmonic metal surface. When the frequency of the evanescent field matches with the frequency of the oscillation of the electrons on the surface, resonance phenomenon is created which gives rise to a CL peak. At resonant condition, highest energy transfer occurs between the core mode and the SPP mode and the real part of their refractive indices matches. A shift in the position of the peak at the resonant wavelength occurs when the variation of the RI of the analyte is observed. This propagates the way for a wide range of analyte detection using SPR-PCF sensors. The effectiveness of PCF-SPR sensors in the THz regime has paved the way for enhanced bio-sensing and improved THz waveguide propagation applications.

The numerical study and proposition of a hollow-core PCF optical cancer detection sensor using Finite Element Method (FEM) in the COMSOL Multiphysics v5.5 environment have been performed that displays an extremely high RS of 99.9314%, 99.9257%, 99.9169%, 99.9277%, 99.9243%, and 99.9302%, with a reduced effective material loss of 8.09×10^{-5} cm^{-1} , 8.79×10^{-5} cm^{-1} , 9.88×10^{-5} cm^{-1}, 8.55×10^{-5} cm^{-1}, 8.96×10^{-5} cm^{-1}, and 8.24×10^{-5} cm^{-1} for breast cancer type-2, cervical cancer, skin cancer, adrenal gland cancer, blood cancer, and breast cancer type-1 respectively at a frequency region of 3.0 THz, while displaying an extremely low confinement loss of 6.1 × 10−10 dB/cm[19]. A sectored circular PCF having topas as background material has been proposed that displays an average sensitivity is 92.14% and CL value of 2.308 $\times 10^{-9}$ cm^{-1} along with EML values of 0.009598/cm for RI=1.33, 0.009620/cm for RI=1.34, 0.009624/cm for RI=1.35, 0.009658 cm-1 for RI=1.36, 0.009694 cm^{-1} for RI=1.37 at 1.5 THZ frequency[20]. Moreover, Rahman et al. conducted the numerical investigation of a with octagonal hollow-cored PCF structure surrounded by symmetrical air holes in the cladding capable of improving the identification of all tested blood components (RBC, hemoglobin, WBC, plasma, and water) by nearly 99 % with the attainment of a negligible CL value of $10^{-16\pm1}$ dB/cm at 4.5 THz operating frequency[21]. Furthermore,

Rahman et al. again proposed a PCT geometry with polarization maintaining attributes while displaying extremely low EML of 0.013/cm and 0.020/cm in modes of x and y-polarization, respectively, a flattened dispersion value of ±0.020 ps/THz/cm and±0.065 ps/THz/cm at frequency of 1 THz in the x and y-polarization modes respectively, and detecting liquid chemicals, such as, methanol, ethanol, benzene, and cholesterol, and air pollutants, such as, dioxin, cyanide, hydrogen sulphide, and nitrogen oxide [22]. Islam et al. have proffered a sensor with hexagonal outlined porous cladding with vacant core with high bi-refringence value, capable of detecting cyanides at THz regime, utilizing Zeonex as the material in the background; the numerical investigation of the proposed sensor being performed using FEM exhibits very high sensitivity of 99.75%, extremely small confinement loss of 0.5×10^{-13} cm^{-1}, and a considerably low and flat dispersion of 0.12 ps/THz/cm[23]. Furthermore, a PCF sensor based on optical fiber with rectangular air holes in both the core and cladding has been demonstrated by Khan et al. which depicts low loss and increased sensitivity for the detection of volatile impurities in Ethanol with the highest efficacy. The simulation performed for the mentioned sensor using FEM exhibited RS of 99.15%, 99.36%, and 99.41% with confinement loss values of 5×10^{-17} dB/cm, 2×10^{-16} dB/cm and 1.17×10^{-17} dB/cm, Effective Material Loss (EML) of 0.00065 cm^{-1}, 0.00085 cm^{-1}, and 0.00068 cm^{-1} for Ethanol, Methanol, and Benzene respectively at 2.2 THz frequency band[24]. The experimentation of a Zeonex based hexagonal packing PCF sensor with a wheeled structure for porosities of 85%, 90%, and 98% in the regions of 0.2 to 2.0 THz has been performed; the sensor is capable of detecting cow and camel milk with RIs of 1.3459 and 1.3423 respectively and has shown the highest sensitivity of 81.16% and 81.32%, EML constituting values of 0.033013 cm^{-1} and 0.03284 cm^{-1}, trivial values of CL of 8.675× 10–18 cm^{-1}, 1.435× 10–18 cm^{-1} for camel and cow milk respectively, a high value of 81.573% for core power fraction, and 0.256 as the numerical aperture value[25]. Moreover, a hexagonal cladding structured, Topas-based PCF sensor with hollow core and air cavities structured with square shapes in both the core and the cladding, investigated through FEM in COMSOL v5.3a software is presented by Islam et al. showing sensitivity of 99.39% for RBC, 99.27% for haemoglobin, 99.12% for WBC , 99.03% for plasma, and 98.79% for water, least CL of 1.124×10^{-15} dB/cm for RBC, 9.557×10^{-16} dB/cm for haemoglobin, 7.242×10^{-15} dB/cm for WBC, 1.114×10^{-16} dB/cm for plasma, and 2.515×10^{-15} dB/cm for water in y-polarization with optimized design conditions in the 2-5 THz frequency range along with optimal characteristics, such as, low EML, high bi-refringence, increased effective area, extensively low and flattened dispersion, and large divergence of beam[26].

Moreover, a PCF biosensor with two hollow air cavities of square shape enclosed by four air channels of rectangular shape residing in the region of cladding has been proposed for an effective detection of amino acids using THz waves and the scrutiny of the sensor's characteristics applying FEM in COMSOL Multiphysics has depicted extremely high RS with values of 99.97% for phenylalanine, 99.98% for tryptophan and histidine, 99.95% for methionine, and 99.93% for lysine, extremely trivial CL values of 4.72×10–22 cm^{-1} for tryptophan along with other mentionable optical propagation properties, such as, low EML, enlarged effective modal area, and flat dispersion with near-zero value for optical design parameters at 3.4 THz frequency[27]. A fabrication-friendly hexagonal shaped THz PCF-based chemical sensor with a core that's hollow and air lattices that are symmetrically hexagonal in the cladding section that exhibits extensively elevated performance in THz regime (almost 99% at 3 THz) for the detection of ethanol, methanol, water, and benzene has also been proffered and the numerical investigation has been performed using FEM in COMSOL Multiphysics v.5.3a[28]. Furthermore, another Topas based PCF sensor with six head star structure, hexagonal shaped hollow core, and fabrication feasibility has been proposed by Mou et al. for methanol detection, which displays extensively high sensitivity of 98.4%, extremely low CL of 3.34×10-19 cm^{-1}, and very low material absorption loss of 0.002 cm^{-1} at 3 THz operating frequency[29]. The performance analysis of an octagonal shaped hollow cored sensor having cladding structure with eight head stars for cholesterol detection in THz frequency regions using FEM in COMSOL Multiphysics has been performed and the proposed sensor displayed very high sensitivity of 98.75 %, CL as low as 3.14×10^{-20} cm^{-1}, and EML value as low as 0.0008 cm^{-1} at the frequency of 2.2 THz [30].

A PCF design with octagonal shaped cladding design for THz transmission has been presented that exhibits an EML as low as 0.007 cm^{-1} at 0.5 THz frequency, an extremely high bi-refringence value of 0.06, a value of about 4×10^{-6} m^2 for effective area, a value of 70 % for core power fraction with a diameter of 290 micro meter for the core having a core porosity of 80% at the frequency regime of 1.6 THz, and a flattened dispersion of variation 0.3 ± 0.1 ps/THz/cm within 0.7–2.1 THz which is a significantly large frequency range of [31]. Besides, Islam et al. proffered a PCF design with slotted core with unsymmetrical air holes structures for the achievement of a high modal bi-refringence of 0.0911 and air holes arranged compactly in five hexagonal layers in the cladding region to attain a low EML value of 0.025 cm^{-1}; the design exhibited core power fraction value of 52%, CL as low as 1.05×10^{-13}/cm, and a flat dispersion of 0.65 ± 0.05 ps/THz/cm in the 0.5 to 1.6 THz frequency range[18]. A fabrication

friendly PCF structure with a square core and four symmetrical air fragments in the cladding section arranged in a circular manner suitable for THz sensing and waveguide application has been demonstrated by Mou et al. where the structure displays extremely low EML of 0.009 cm^{-1}, near zero 0.35 ps/THz/cm flattened ± 0.05 ps/THz/cm dispersion for waveguide operation at 1 THz, an enhanced effective area of 9.56×10^{-7} m^2, and a core power fraction as high as 53.159% at optimal design conditions. Additionally, the PCF design is capable of detecting toxic environmental pollutants with an incredible proportion of 91.5 %, 89.8 %, 89 %, 89.5 %, and 89.6 % for dioxin, toluene, hydrogen sulfide, nitrogen dioxide, and sodium cyanide respectively[32]. Rahman et al. have proposed another Topas based PCF geometry where core and cladding are compartmentalized by a few number of rectangles with air fragments of core and cladding arranged in a circular manner for ease of fabrication; numerical investigation using FEM in COMSOL Multiphysics v.5.3a depicted an extensively low EML of 0.0153 cm^{-1}, extremely flat dispersion of ± 0.010 (ps/THz/cm), an ultra-low confinement loss of 0.0014 cm^{-1} at optimum 1 THz operating frequency, and an extensively flattened dispersion variation of ± 0.01 (ps/THz/cm)[33].

Furthermore, Islam et al. have proposed a hollow cored Zeonex based PCF structure with an enhanced level of cladding asymmetry introduced by using a brick-like structure with

identical square shaped air cavities and numerical investigation of the proposed fibre using FEM in COMSOL Multiphysics v.5.3 showed very high sensitivities of 98.6%, 98.7%, 98.8%, 98.83% and 98.9%, and ultra-low confinement loss of 5.5×10^{-9}/cm for RI=1.33, 3.25×10^{-9}/cm for RI=1.34, 1×10^{-9} /cm for RI=1.35, 7.75×10^{-10}/cm for RI=1.36 ,and 5.5×10^{-10}/cm for RI=1.37 at optimal design conditions along with other favourable propagation characteristics, such as, enlarged effective modal area, very high birefringence, and an extremely low EML[34]. Rahman et al. has presented another air cored 45^0 rotational square lattice PCF design for THz waveguide which gives very low EML values of 0.016 cm^{-1} and 0.013 cm^{-1} at 1 THz and 0.8 THz respectively, and an average core power fraction of around 40 % for core porosity of 81% in the frequency range of (0.6 to 1.8) THz with the highest core power fraction being 58.88%[35]. A porous core rotate hexagonal PCF structure has been proposed for the purpose of increasing the efficiency and reliability of THz transmission and the numerical analysis of the design using FEM and PML displayed an ultra-low EML of 0.049 cm^{-1}, an extremely high power fraction of 43% at an operating frequency of 1 terahertz, around zero extensively flat dispersion, and single mode properties[36]. Similarly, a Topas based PCF design consisting of only rectangular slots has been presented whose numerical analysis using

FEM demonstrated significant properties, such as, a flat dispersion of 0.22 ± 0.01 ps/THz/cm, a low value of EML ranging from 0.009/cm to 0.01/cm in the range of frequency of 0.77–1.05 THz, a high birefringence, single mode operation, and extremely low confinement loss which ensures the efficient transmission of THz signals by preserving their polarization[37]. For the purpose of application in THz range, a hybrid cored, fabrication friendly PCF with only circular air holes in the core and the cladding has been proffered that exhibits an extremely low confinement loss of 10^{-3} cm^{-1}, an extensively low EML of 0.035 cm^{-1} due to the bulk absorption loss of Topas, a flat dispersion with an almost zero value of 0.07 ps/THz/cm for operation in single-mode[38].

Again, with a view to ensuring polarization maintaining applications in THz transmission, a PCF geometry potentially to be fabricated by implementing the capillary stacking and sol-gel technique and consisting of octagonal cladding structure has been investigated for THz wave-guidance that concurrently depicts a significant birefringence value in the 0.8-1.05 THz frequency range with single mode operation, the birefringence value being ~0.043 at 0.73 THz operating frequency due to the prevailing unsymmetrical structure in the core arising by the coexistence of both elliptical and circular air holes, and a trivial EML value of 0.044/cm[39]. A PCF design with elliptical array shaped core with rectangular cladding has also been proposed for the purpose of polarization maintenance and multi-channel communication of THz waves; the simulations from the proposed design using FEM displayed a high birefringence value of 0.063 at 1.5 THz due to asymmetry of air holes in both core and cladding, an EML as low as 0.06/cm at 0.6 THz, an extremely flat dispersion variation of plus minus 0.02 ps⁄THz⁄cm in the 1.05–1.5 THz frequency range due to compact geometry and different air hole sizes in the cladding, and 46% as the core power fraction value at 1.1 THz for y-polarization[40].Another Zeonex based PCF design with Kagome lattice, diamond shaped core with porous structure has been proffered for the purpose of both polarization maintenance and biomedical imaging applications in THz regime whose numerical analysis using FEM shows a high numerical aperture of 0.48, a high birefringence value of 0.039, a negligible EML of 0.078/cm at 1.1 THz, a flattened dispersion of 1.07 ± 0.05 ps/THz/cm, , and a CL as low as 1.39×10^{-4}/cm for 30 % porosity at x-polarization mode[41].

For the purpose of efficient THz transmission, a porous-core circular PCF, also termed as PC-CPCF, has been designed, was simulated using full vector FEM and PML, and its outcomes were a low EML value of 0.043 cm^{-1} , an acutely high core power fraction of 47%, an overly flattened dispersion variation of 0.09 ps/THz/cm, and a confinement loss with a trivial value

of $10^{-2.5}$ cm^{-1} along with single mode operation properties[42]. Moreover, for THz wave guidance, a Topas based hybrid porous core octagonal lattice PCF has been numerically investigated using full vector FEM and displays an EML as low as 0.04 cm^{-1}, maximum core power fraction of 50.4% at a core diameter of 350 μm and operating frequency of 1 THz at 81% porosity, and an acutely flattened dispersion of 0.10 ps/THz/cm within the frequency range 0.95–1.15 THz[43]. For polarization maintaining guidance of THz waves, an investigation of the numerical properties of slotted-porous core microstructure polymer fiber was performed that showed a high modal birefringence of ~0.08 because of the existing asymmetry inside the core introduced by rectangular slotted air holes, a very low EML of ~0.08 cm^{-1} for 35 % porosity and core diameter of 350 μm at 1 THz frequency, a flat dispersion value of 0.85±0.05 ps/THz/cm for y-polarization in the frequency range of 1.16-1.5 THz[44]. Additionally, a porous-core octagonal photonic crystal fiber (PC-OPCF) is proposed for THz transmission that displays a low EML value of 0.047 cm^{-1}, a power transmission of 49% through core air holes, and a flattened dispersion variation of 0.15 ps⁄THz⁄cm at 1 THz operating frequency and a core diameter of 345 μm when its numerical analysis has been done in COMSOL Multiphysics v4.2, and making it an efficient medium for THz wave transmission[45].

A novel PCF Biosensor with high sensitivity in the region covering the visible and near-infrared (IR) bands and fabrication-friendliness is proposed in this study which comprises of a singular lattice layer of hexagonal shape comprising air-slots of only circular structure. The suggested design has an x-polarization mode sensor resolution of 2.4×10^{-6}, a peak WS of 41,000 $nmRIU^{-1}$, and a maximum AS of 1072.5 RIU^{-1}[46] Recent years have seen a substantial increase in interest in the use of photonic crystal fibers to detect alcohol in beverages. Islam et al. proposed a novel Zeonex-based PCF for alcohol detection, which exhibited remarkable characteristics in the terahertz frequency band. The fiber was characterized using the FEM, and results of simulation showed a remarkable RS value of 88.6%, as well as a very low EML of 0.0222/cm, and negligible CL of 3.63 10^{-11}/cm at 1.9 THz operating frequency[46]. Using comparative analysis of AS as the metric of sensitivity, the first study that suggested a biosensor for identification of blood components in the frequency regions comprising of the near-infrared and visible spectrum bands demonstrates higher AS of 5078.99 RIU^{-1}. In this case, Al-doped ZnO is taken into consideration as a plasmonic material to boost sensor performance and design extensibility [47]. SPR based PCF sensors have made incredible progress during the past ten years. Islam et al. [30] presented a straightforward circular SPR-

PCF sensor with x-polarization mode. The proposed sensor's maximum AS and WS values are 1757.3 RIU^{-1} and 32,000 $nmRIU^{-1}$, respectively. The design they have proposed also depicts significantly low value sensor resolution value of 1.428×10^{-6}, 587.2 as FOM value, and maximum birefringence of 0.004.

New directions in sensing research have been made possible by the coupling of PCF sensors with plasmonic materials. Due to its stability and chemical inertness, gold is a material that is highly favoured in the plasmonic field. Because they may be made using common methods like stack and draw and still offer great sensitivity, simple and easily constructed structures are very desirable. Islam et al. presented a number of unique solid core photonic crystal fibers in their study that are intended to take advantage of the surface plasmon resonance (SPR) phenomena. These fibers were designed with a specialized circular cladding structure that not only made manufacturing them easier but also improved their sensing capacities[48]–[50]. The geometric properties of the photonic crystal fiber (PCF) can affect the sensor's performance since they have a direct bearing on how the plasmonic layer surface interacts with the evanescent field. The square lattice design is widely regarded as the easiest to construct lattice structure. The insertion of annular airholes in the square lattice has shown to be a noteworthy improvement in the context of biosensors, demonstrating outstanding sensitivity and resolution[48]. Specifically, for biological sensing applications, a unique structure with two arrays of six small airholes on each side and two arrays of two large airholes on each side displayed higher sensitivity. When compared to other structures, this particular design produced a higher level of sensitivity, making it an attractive option for biomedical sensing applications[49]. The addition of airholes with the same radius has considerably simplified the production of the biosensor design. With this design decision, the core mode and plasmonic mode may more easily couple, which facilitates efficient coupling and results in high amplitude and wavelength sensitivity. The regularity in the size of the airholes ensures the biosensor's reliable and optimal performance[50]. The use of a hexagonal lattice structure with a greater quantity of rods in the context of surface plasmon resonance (SPR)-based photonic crystal fibers (PCFs) enables additional versatility in design for both the core and cladding. This structural design gives the PCF more control over its optical properties and capabilities, allowing for better performance in SPR applications for sensing. The greater the number of rods, the easier it is to manipulate the modal properties and interact with the plasmonic layer, resulting in both increased sensitivity and efficiency of the PCF- SPR sensor[46], [51]–[54]. In the biosensor's cladding region, an intelligent arrangement of air holes, including hexagonal-

shaped groups and v-shaped configurations, has been applied[51]. The development of four channels for efficient light transmission from the core to the plasmonic mode is facilitated by these air holes of a specified dimension. The cladding's clustered pattern of circular-shaped air spaces contributes to improved plasmonic effects. The use of an Al-doped ZnO (AZO) coating as the plasmonic material improves the performance and flexibility of the design of the sensor. The modified design has better amplitude sensitivity, resolution, and FOM. The inclusion of an extraneous AZO layer to the sensor construction improves design flexibility and optical tuning that outperform the metal films used traditionally[52]. The use of a TiO2 coating and a novel twin spider core arrangement in a biosensor design led to better gold adhesion to the fiber[53]. A unusual structure consisting of two clusters that are V-shaped generating the shape of an eye is used in the cladding section of one design. These clusters have a symmetrical arrangement along a horizontal line in the opposite direction. A thin gold layer with an island pattern of development is used to improve the sensor's performance. A carefully aligned ring-shaped layer is also used to decrease surface exposure effects[55]. One sensor can sense analyte, magnetic field, and temperature by the virtue of a new trigonal cluster-based configuration of circular air holes within the fiber that enables effective interaction with the environment[56]. In a study, a square lattice and solid core SPR-based PCF sensor with extremely low loss and appropriate sensitivity are proposed and examined. Along with its ability for magnetic field and temperature detection, the sensor also exhibits an exceptionally high external strain sensitivity of 4.00 pm /με[57]. In a study, a dual cluster and dual array design is used for the suggested structure. In order to successfully direct the electromagnetic (EM) wave to the surface and improve the overall sensing performance, the air holes within the fiber are strategically placed[58]. There are significant gains in performance metrics with the suggested PCF design, which has elliptical air holes and a perfectly circular shape[59]. When the elliptical, rectangular, and circular air holes that were developed are compared, it is found that they produce the best outcomes. In one study, the centre airhole was purposefully chosen to be rectangular rather than the more typical circular shape in order to create birefringence. This innovative design decision causes asymmetry in the structure of the photonic crystal fiber, which results in an altered reaction to polarization and increased birefringence[60]. To induce birefringence in the photonic crystal fiber, another design comprises hexagonally arranged clusters of circular airholes in the cladding, as well as a rectangular airhole in the middle[61]. It is noteworthy how PCF-SPR sensors are applied in communication. In a D-shaped PCF with a micro-opening, a unique broadband single-polarization filter has been successfully developed using SPR[62]. The advancement of SPR-

PCF has found a new direction with the implementation of double resonance using two plasmonic materials[63]. The simultaneous use of two materials using localized surface plasmon resonance has been used to enhance the detection range of the sensor.

In this work, we have proposed an LSPR based PCF sensor that uses the concurrent application of gold and GZO in order to create two peaks at two distinct wavelengths. The evolution of two peaks occurs due to the splitting of the evanescent field as it interacts with the surface plasmons. Our proffered sensor introduces a broadened working range both in the ultra-violet and the visible spectrum range which was never observed in any of the literatures stated above. Therefore, the uniqueness, efficacy, and novelty of the sensor for the diverse biosensing field can be strongly established.

CHAPTER 3

PHOTONIC CRYSTAL FIBER

3.1 Introduction

Optical fiber is the leading choice for information transmission due to its ability to guide light. To meet the growing demands of the Internet, a new generation of fibers has been developed with improved propagation characteristics, including reduced losses and enhanced performance compared to traditional fiber. Among the optical fibers Photonic Crystal Fiber (PCF) has exceptional waveguiding capabilities. When compared to standard optical fibers, it has a greater ability to restrict light. PCFs are typically made of a microstructure arrangement with undoped silica as the backdrop material, and air holes run the length of the fiber. The central portion is known as the core, while the region surrounding the core is known as the cladding. The backdrop material is not only limited to undoped silica different kind of crystal fiber materials maybe used for different applications. For example porous core combined with TOPAS base material gives great relative sensitivity at very low confinement loss, making it suited for practical chemical sensor applications[64]. Because of its high flexibility and the ability to create longer PCFs, Teflon has been employed as a background material [65][66]. Some other crystal fiber material are GaAs, PMMA and Arsenic Sulphide which are used for beam splitter application of PCF[67]. There are wide range of PCF applications such as fiber optic interchanges, fiber lasers, non-linear devices, high control transmission, various gas sensors, data transmission in the THz regime, and so on. The structure of core and cladding regions of a PCF also help to enhance the performance of the sensor and also applications may vary. Initially Tarunnum Parvin et al [68] presented a PCF sensor with a circular core region and closely bound hexagonal air holes in the cladding area for the detection of TB cells. Later on Jesper Laegsgaard proposed honeycomb cladding structure[68]. For the flexibility , advanced use and fabrication other designs of core were implemented like circular[69], square[70], octagonal[71], spiral[72], D-shaped[73] and hybrid[74]. It has been discovered that the fiber core of photonic crystal fiber (PCF) sensors can be engineered to have a large mode field diameter, enhancing the interaction volume between light and samples and improving sensitivity. As a result, we can see that there are a ton of PCF designs that are feasible and that photonic crystals can produce effective results.

3.2 Photonic Crystal Fiber in Brief

Photonic crystal fibers use the idea of photonic bandgaps to control and manipulate light in novel ways, in contrast to conventional optical fibers that rely on index guiding for light propagation. A solid core encircled by a cladding layer consisting of dielectric materials with various refractive indices makes up conventional optical fibers. The core region is doped with high index material compared to the cladding region. Usually Silica which has lower refractive index been used in cladding and Germanium is used to increase the refractive index. On the contrary, Fluorine is usually used to decrease the refractive index.

Photonic crystal fibers have a more intricate structure. They are made up of a solid or hollow core that is encircled by a cladding zone that is periodically perforated by airholes or high-index materials. A photonic bandgap is produced by this periodic structure, which may prevent light from traveling in some directions or at certain frequencies. The low loss dielectric medium constructed with periodic array of microscopic airholes spans throughout the entire fiber length. In PCF, the core guidance of optical signal is achieved with solid silica core and the photons are provided with better waveguides than conventional optical fiber. A perennial air-hole array in the cladding surrounds this core which has lower refractive index than the core. Because of this refractive index difference the light signal can be guided by total internal reflection along the silica induced core. The core is typically created by adding a larger air hole in its place or removing an air hole from the center of the construction.

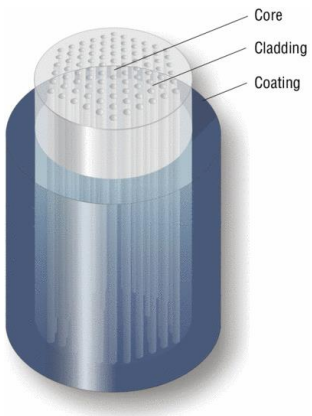

Fig 3.1 Photonic Crystal Fiber

3.3 Classification of PCF

In PCF the light is entrapped unlike conventional optical fiber where the refraction phenomena is used for the light waves to travel across the core region. The longer the propagation distance,

the more the transmission loss increases. So, repeaters and amplifications must be ensured for long-distance better-quality communication. In case of PCF as the light waves are entrapped which gives better waveguide propagation also flexibility is provided in background material. Also, the production cost is less compared to Conventional optical Fibers.

Photonic crystal fibers (PCFs) can be categorized according to a number of things, such as their structural layout, guiding system, and applications. Here are some typical divisions of PCFs:

1. Structural Design:

   a. Solid-core PCF: These fibers have a solid core encircled by an airhole- or pattern-arranged high-index cladding region.

   b. Hollow-core PCF: These fibers have a hollow core that is filled with air or gas and is encased in a cladding structure. Hollow-core PCFs can be further divided into inhibited coupling fibers and photonic bandgap fibers.

2. Guiding Mechaninism:

   a. Index-guiding PCF: These fibers, like normal optical fibers, use the difference in refractive index between the core and cladding to guide light.

   b. Photonic bandgap PCF: Based on the periodic structure of the cladding, these fibers use the photonic bandgap effect to restrict and guide light within the core region.

3.4 High Index Guiding Effects

Photonic crystal fibers are quite different from traditional optical fibers since this portion of the cladding is highly wavelength dependant and not identical to pure silica. We may create limitless single-mode fibers that only allow a single mode regardless of wavelength because the refractive index is substantially wavelength dependant. Total internal reflection is referred to as M-TIR when referring to optical fibers. They rely on a core with a high index, often made of pure silica, and an outside microstructure that has a low index of refraction. The ability to readily alter the dispersion characteristics of the fibers, allowing us to create optical fibers with an irregular dispersion characteristic at visible wave lengths. Today, it is possible to design optical fibers with an irregular dispersion characteristic at visible wave lengths by controlling the refractive index profile, resulting in optical fibers with large mode-field diameters and higher beam quality fiber guidance and amplification

3.5 The Band Gap Effect

The band gap effect in photonic crystal fibers (PCFs) refers to the phenomena where specific light frequencies are prevented from propagating in particular directions within the fiber. It is comparable to the band gap in electronic materials' energy band structures. Photonic bandgaps are created by the strategically placed microstructure in the cladding region of PBG fibers. The core region in PBG fibers are formed by creating defects in the structure of the fiber which enables a photonic band structure. Photonic band structure comprises of bands or frequency ranges forbidden or allowed. Light rays at particular frequencies cannot go through the fiber in specific directions inside the band gap. It can only pass through low indexing mode. In conventional optical fibers we cannot expect this type of advantage which opens large potential possibilities like through the fiber's substance, we can direct light waves through any compatible gas or the air.

3.6 Hollow Core and Solid Core

Hollow core and solid core are 2 kinds of special class PBG fibers. Both utilizes the bandgap effect to confine and guide light within the core region

Hollow core photonic bandgap fibers (HC-PBGF) contain a hollow core and a cladding structure with airholes or high-index materials spaced out periodically around it. Since the cladding is periodic, a bandgap is formed that prevents some frequencies from traveling in a particular direction. A core made of air contains the electromagnetic field. But unlike other photonic bandgap fibers, light is only steered in a small spectrum through air-core fibers. The typical bandwidth for fibers guiding at 1550 nm is 200 nm. The anti-guiding core region is located below this region. Low nonlinearity, broadband transmission, lessened light dispersion, and flexible light guidance are just a few benefits of hollow core fibers. These fibers exhibit fewer nonlinear effects because of their hollow core architecture, which enables high-power laser transmission. They are appropriate for applications demanding precision pulse timing, dispersion management, and customized mode attributes because they offer broadband transmission over a wide range of wavelengths and enable exact control over guided modes. However, producing hollow core fibers can be difficult, and they might have greater losses than solid core fibers, particularly at longer wavelengths.

In Solid core photonic bandgap fibers (SC-PBGF) the cladding is made up of a periodic structure that produces a bandgap effect, and the core is a solid substance. The bandgap

confines the light inside the solid core by preventing some frequencies from traveling in some directions. SC-PBGFs are well suited for single-mode fiber lasers, supercontinuum production, and high-resolution spectroscopy because they have features including high mode confinement and low nonlinear effects. By combining the filtering effect with a core doped with a rare earth substance like Yb at a newer wavelength with a smaller fiber gain, the process of amplification and lasing can be done easily. The laser community has a wide range of options thanks to the doped-solid-core photonic bandgap fiber and the particularly dispersive properties.

3.7 Fiber Bragg Grating

Fiber Bragg Gratings have gained immense popularity for detecting analytes based on RI and biolayer thickness[75]. They are utilized not just for conventional sensing functions like temperature, strain, and pressure measurement, but also for gauging the thickness of biological layers. A spectral-based modality, or wavelength shift approach, is what the FBG relies on for sensing. The Bragg wavelength is influenced by the grating time and effective refractive index[76]. The central Bragg wavelength is shifted by the grating period and effective refractive index. It is possible to detect a wavelength change under the Bragg condition, which indicates how much external perturbation has been applied to the FBG. Changes in the central wavelength can be found using the optical spectrum analyzer (OSA). Time division multiplexing (TDM), spatial division multiplexing (SDM), wave division multiplexing (WDM), and frequency modulated continuous wave (FMCW) multiplexing techniques are used when several sensors are required. Normal uniform fiber Bragg gratings (FBGs) must have their cladding partially or entirely etched in order to increase their sensitivity to changes in the external refractive index. The interface between the fiber and the external medium is improved, which makes FBGs more suitable for applications involving the detection of refractive indices. The most popular technique for measuring strain uses a Wheatstone bridge circuit to measure the change in resistance brought on by induced strain. As silica material functions at a low-temperature range, strain detection at high temperatures can be quite difficult for FBG. Modern sensor technology makes extensive use of polymer-based optical fibers because of their high breakage limit and biocompatibility. Fiber Bragg grating-based sensors feature great EMI immunity, low thermal conduction, and high reliability. They are also compact and have low thermal conductivity. Temperature sensitivity in FBG is mostly caused by the thermo-optic effect.

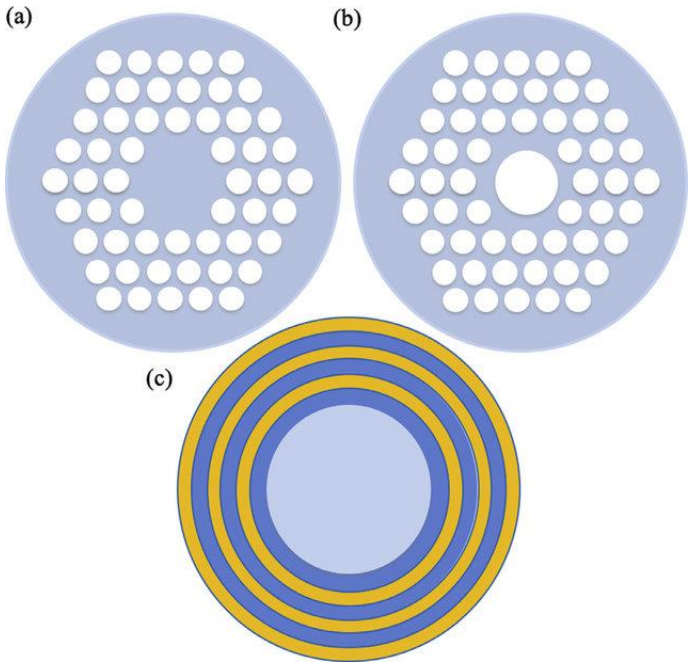

Fig 3.2 (a)Solid Core PCF (b)Hollow Core PCF (c)Bragg Fiber

Photonic crystal fiber (PCF) has a tremendous potential for a wide range of applications because of its special qualities and tunable transmission characteristics. The amazing flexibility and adaptability of PCF is due to its tunable optical features, which include the ability to regulate the core and cladding. Due to PCF's intrinsic adaptability, its performance can be customized to meet the needs of certain applications.

CHAPTER 4

SPR AND LSPR BASED PCF SENSORS

4.1 Surface Plasmon Resonance

4.1.1 Introduction

Surface plasmon resonance (SPR) is a phenomenon that happens when light interacts with a metal-dielectric interface, usually involving noble metals such as gold or silver. It is a potent technique used in various fields, including physics, chemistry, biology, and materials science, for studying the interactions between biomolecules, analysing thin films, and detecting analytes. SPR sensors have previously been used in a wide variety of real-world applications, including bio detection , environmental monitoring, food safety, medical diagnostics, temperature sensing, strain sensing, gas detection, and water testing[77]–[79]

4.1.2 Working Principle

The interaction between light and surface plasmons at a metal-dielectric contact is the foundation of surface plasmon resonance (SPR). SPR is typically measured using the Kretsch-man configuration, which consists of a prism and a thin layer of a highly reflective metal (such as silver or gold) put on the base of the prism [77] .Surface plasmons are activated by shining light at a particular angle and wavelength onto a thin metal layer, producing an evanescent wave that interacts with molecules close to the surface. Analyte characteristics like concentration, kinetics, and affinity can be determined via observable variations in the resonance angle or reflected light intensity caused by changes in the refractive index brought on by molecular binding or interactions. A change in the reflectivity bend indicates an atomic official event that is occurring on, near, or in the metal film, as well as a conformational change in the atoms bonded to the film. Analysts can think about atomic official occasions and official energy without the hassle of a term by comparing this movement to time.

4.1.3 Reason of Interest

Due to the wide range of applications for SPR, optical fiber-based SPR sensor technology has been widely used in industries like food quality detection, chemical analyte analysis, magnetic field detection, and environmental measurements in the recent years. Compared conventional optical fibers, SPR based optical fibers exhibit low cost, compact size which enables applications in narrow spaces, also high degree of integrations enabling distributed and real time measurements. In 1993 first SPR based optical sensor was proposed by Jorgenson et

al[77] . In recent advancement in technology also created great interest in SPR based PCF due to sensor prompt response, flexible design, high sensitivity, and birefringent characteristics making it capable of variety of sensing applications[80]–[82]

4.1.4 Surface Plasmon Wave

Surface plasmon wave, sometimes referred to as a surface plasmon polariton (SPP), is the collective wave of oscillating electrons that propagates along the metal-dielectric interface. Surface plasmons are excited when light with the right frequency and angle contacts with a metal surface. This causes a propagating wave to form along the interface. It is highly sensitive to refractive index and the main basis of SPR Due to its special features and capacity to contain and control light at nanoscale scales, surface plasmon waves can be employed for a variety of purposes, such as sensing, waveguiding, and subwavelength imaging.

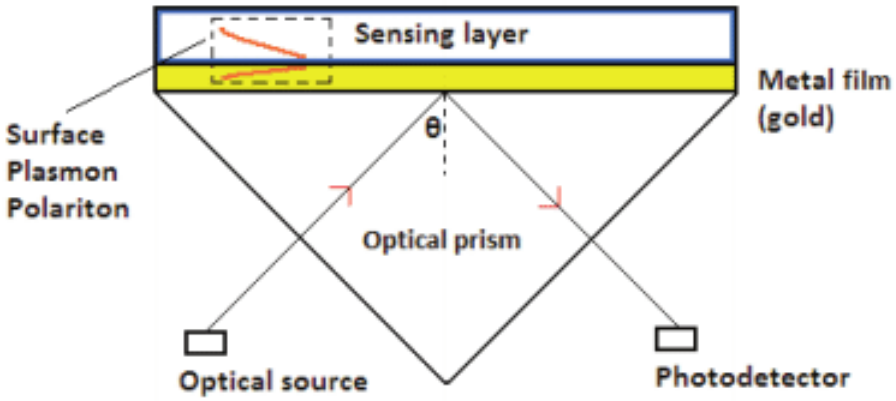

Fig 4.1 Surface Plasmon Wave

4.1.5 Evanescent Field

Evanescent Field is an exponentially decaying electromagnetic field with respect to the distance from boundary and exists only close to the interface between two media with different refractive indices. Because they interact with molecules or other materials nearby the metal surface, evanescent fields are crucial in SPR. Changes in the evanescent fields' intensity or phase as a result of this interaction can reveal details on molecule binding activities, thin-film characteristics, or other processes taking place close to the interface. SPR allows for sensitive and label-free detection of molecular interactions as well as the characterization of thin films by detecting and examining these evanescent fields. The ability of the evanescent wave to

spread into materials around the fiber core beyond the core boundary can be taken advantage of by removing the fiber cladding.

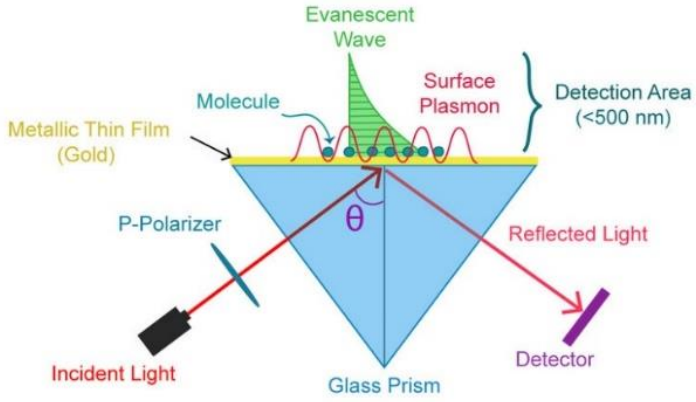

Fig 4.2 Evanescent Field

4.1.6 Implementation of SPR

SPR has a wide range of applications , recently it gained acknowledgement as a biosensor D. Irawana et al [80] proposed a SPR based PCF sensor for early detection of infected skin cancer cells and healthy cells. Also SPR has shown considerable potential, particularly in identifying low molecular weight environmental dangers in complicated matrices[83].In various range of Biosensors , Optical Biosensors SPR has created a new dimension because of its label free and real time sensing characteristics[84] .Also SPR based chip was also proposed for Covid19 detection because of its fast ,accurate detection in Biomolecular[24], [85].

4.1.7 Advantages of SPR

- ✓ Label-free Detection: One of the major benefits of SPR is its capacity for label-free detection. Since fluorescent or radioactive labels are not required, no extra chemical alterations or labeling procedures are necessary. This streamlines the testing process and lessens the possibility of label artifacts or interference.
- ✓ Real time and kinetic analysis: Kinetic analysis and real-time monitoring of molecular interactions are made possible by SPR. It enables the investigation of kinetics, affinities, and binding constants by allowing the measurement of binding events as they take place. This ability is very helpful for researching quick or dynamic interactions and figuring out how quickly biomolecules bind.

- ✓ Sensitivity: SPR is a highly sensitive technology that can identify molecule interactions at concentrations between picomolar and femtomolar. A metal-dielectric interface provides exceptional sensitivity for detection and quantification because changes in refractive index there are directly proportional to the presence or quantity of analytes.
- ✓ Versatility: Small molecules, proteins, nucleic acids, and carbohydrates are just a few of the analytes that can be studied using the flexible SPR approach. It can be used to investigate a variety of interactions, including DNA hybridization, antigen-antibody binding, protein-protein interactions, and enzyme-substrate interactions. Additionally, SPR is applicable to both liquid and gas phase settings, making it flexible for use in a variety of experimental configurations.
- ✓ Realistic Experimental Conditions: SPR can be performed under physiologically relevant conditions, such as in aqueous solutions or complex biological matrices like serum or cell lysates. This allows for the investigation of biomolecular interactions in conditions that closely mimic the native environment, providing valuable insights into biological processes.
- ✓ High-throughput Capabilities: SPR can be integrated into high-throughput screening platforms, enabling the analysis of multiple interactions simultaneously. This accelerates the data acquisition process and makes it suitable for applications such as drug discovery, protein-protein interaction studies, and biomarker screening

4.1.8 Success Rates and Drawbacks of SPR

The high success rate of high sensitivity SPR provides a specific justification for using it. Small molecule drug development is expensive and takes a long time. Due to other sensors' poor performance, new approaches must be developed and adopted to swiftly and precisely measure their activity. The SPR biosensor technique, however, also has a number of drawbacks. Remember that biosensors require the presence of biologically active chemicals as a starting point. Contrary to other analytical techniques like mass spectrometry or UV spectrometry, which may be used to characterize the material whether it is properly folded and active or not, biosensors require the molecule to be active in order to produce a signal. Despite the fact that biosensor devices are generally simple to operate, developing and implementing.

The integration of Photonic Crystal Fiber (PCF) sensors with Surface Plasmon Resonance (SPR) sensors is an important development in the field of sensing technology. Combining these two potent methods improves sensing capabilities and creates new opportunities for applications across a variety of industries.High sensitivity, low loss, and controlled modal

characteristics, among other distinctive qualities of PCF, offer a strong basis for effective light propagation and interaction with the surrounding medium. SPR is used because it is highly sensitive to changes in refractive index and enables label-free and instantaneous analyte detection.

4.2 LOCALIZED SURFACE PLASMON RESONANCE

4.2.1 Introduction

Surface plasmon resonance (SPR) and localized surface plasmon resonance (LSPR) are closely related phenomena, however LSPR takes place at the nanoscale as opposed to the macroscopic level. The collective oscillation of electrons contained in metallic nanoparticles or nanostructures is referred to as LSPR. These nanoparticles or nanostructures' plasmons resonant when activated by light of particular wavelengths, creating stronger electromagnetic fields around the nanoparticles. Additionally, it has been discovered that the resonance frequency of noble metal nanoparticles strongly depends on their size, morphologies, and even the refractive indices of the surrounding media[86]

4.2.2 Working Principal of LSPR

Based on the interaction between light and the collective oscillation of electrons in metallic nanoparticles or nanostructures, localized surface plasmon resonance (LSPR) is a technique. In contrast to its propagating SPR counterpart, localized surface plasmonic resonances (LSPR) produced by nanoparticles have reduced surrounding refractive index (SRI) sensitivities.[87]. LSPR has shorter electromagnetic field decay length than the SPR ones. These nanoparticles interact with light of a certain wavelength, which excite surface plasmons and create stronger electromagnetic fields around the particles. The LSPR reaction, which is dependent on the size and form of the nanoparticles, is extremely sensitive to changes in the immediate surroundings. LSPR-based sensors may detect and quantify analytes through variations in the LSPR signal by functionalizing the nanoparticle surfaces, opening up possibilities for applications in sensing, detection, and spectroscopy[88][89]

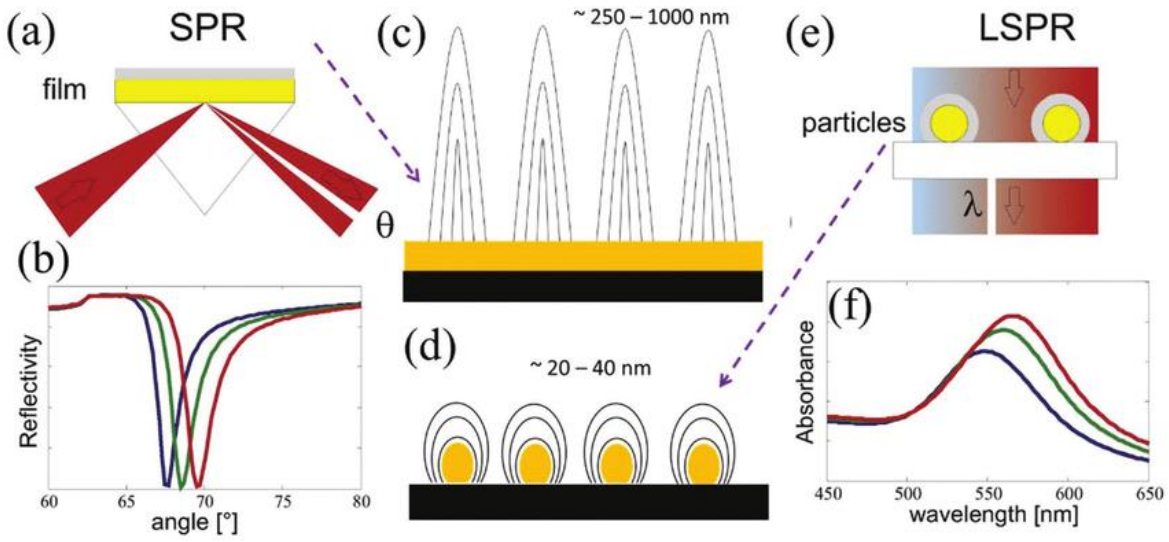

Fig 4.3 Localized Surface Plasmon Resonance

4.2.3 Application of LSPR

The term "localized surface plasmon resonance" (LSPR) is used in many different domains. Sensitive and label-free analyte detection is made possible by LSPR-based sensors, which are used in environmental monitoring and medical diagnostics. Highly sensitive and label-free biological and chemical analyte detection is possible with LSPR-based sensors. LSPR sensors have the ability to measure analyte concentrations, assess binding kinetics, and detect biomolecular interactions by functionalizing the nanoparticle surfaces with particular receptors, such as antibodies or DNA probes. In a recent work Liu et al[90] proposed LSPR based biosensor to simultaneously detection of molecular interactions occurring on the sensor surface. Through LSPR-induced localized heating, LSPR-active nanoparticles, such as gold nanorods or nano shells, can transform light energy into heat. Plasmonic photothermal therapy has made use of this characteristic. Local surface plasmon resonance (LSPR)-enhanced oxygen evolution reaction offers ground-breaking prospects for the development of solar energy conversion.[91]. The wide range of applications LSPR that show its promise for breakthroughs in a variety of domains, including sensing, spectroscopy, treatment, nanophotonic, imaging, and catalysis. LSPR is still undergoing development and study.

4.3 SPR BASED PCF SENSORS

4.3.1 SPR Based PCF Sensors

PCFs are advantageous for a variety of applications, including sensing, because to their distinctive structure, which makes them exhibit a number of fascinating optical features. Unlike conventional fiber-based sensors, PCF-based sensors offer higher sensitivity and minimal resonance peaks, which enhances detection of an unidentified analyte. PCF sensors can attain better sensing properties by adjusting variables like bore of air holes, pitch, and the sum total of the number of rings and air holes of myriad structures.

The interaction between light travelling through the fiber and a plasmonic metal surface is how SPR-based PCF sensors work. When the induced evanescent field interacts with the free electrons on the metal surface, surface plasmon waves (SPWs) are excited. A sharp resonance peak is generated by attaining a phase-matching condition between the SPW mode and the fiber's core mode at a particular wavelength. The resonance wavelength of this peak is very sensitive to variations in the analyte's refractive index. Unknown analytes can be located by tracking this shift and comparing their various refractive indices. PCF-based sensors using SPR technology enable increased sensitivity, accuracy, and adaptability in the detection and characterization of unidentified analytes. High-performance sensing applications now have more options due to the development of PCF-SPR sensors.

4.3.2 Prism Based Sensors

One of the earliest and most popular configurations of surface plasmon resonance (SPR) sensing is prism-based SPR sensors. The coupling element of these sensors, which activate surface plasmon waves at a metal-dielectric contact, is a prism. In 1983 Liedburg first proposed a prism based SPR sensor for gas detection[78]. Later, it was realized that prism-based SPR sensors had some drawbacks, including inaccurate sensing application and bulky size due to additional sophisticated opto-mechanical elements, rendering them unsuitable for remote sensing.[92]

4.3.3 Internal Sensing Sensor

Internal sensing-based sensors, sometimes referred to as intracavity sensors or cavity-enhanced sensors, are a kind of optical sensing technology that uses modifications to the characteristics of light inside a cavity to identify and quantify analytes or physical parameters characteristics of light inside a cavity to identify and quantify analytes or physical parameters[93].It shows more resolution Internal sensing shows higher resolution than external sensing . Filling the interior fiber holes with analytes and covering them with metal coatings is difficult because of small size holes. Additionally, it is impossible to keep the holes' equal thickness during fabrication.

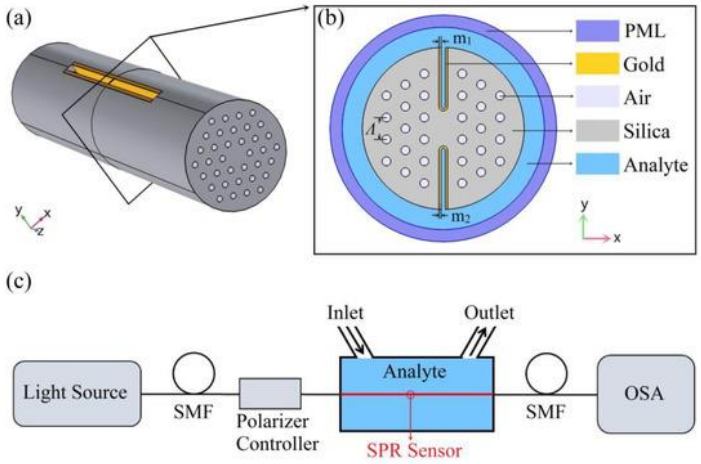

Fig 4.4 Working Principle of Internal Sensor

4.3.4 External Sensing

The sensing element or the interaction zone in external sensing sensors, also referred to as external cavity sensors or external-cavity-based sensors, is situated outside the cavity or resonator. To detect and quantify analytes or physical parameters, these sensors make use of variations in the characteristics of light that take place outside the cavity. The analyte or parameter to be detected is positioned adjacent to the cavity or interacts with the cavity output in external sensing devices, which typically have a cavity or resonator made of reflective surfaces or mirrors. The target analyte or parameter is then determined by analyzing the changes the analyte has caused in the optical characteristics of the contact region. It doesn't need any pre-steps before sampling because the metal coating is outside the fiber as opposed to internal sensing, where the metal coating is inside the air pores. The sensor only needs to stick to the analyte solution, and within a short period of time, it will display the desired sensor performance.

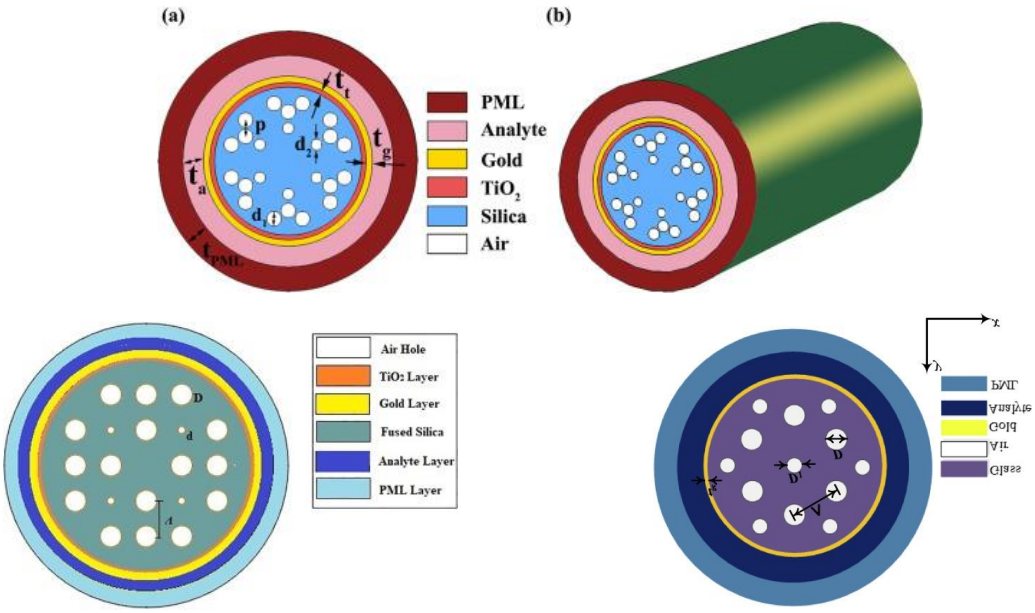

Fig 4.5 Examples of External Sensors

4.3.5 D shaped PCF

A PCF-based sensor with a D-shaped geometry or cross-section is known as a D-shaped photonic crystal fiber (PCF) sensor. It is made by altering the PCF's design to include a flat side that resembles the letter "D". Prism-based sensors' and internal sensing-based sensors' drawbacks can be mitigated by using D-shaped or exposed-core PCFs[94]

CHAPTER 5

PERFORMANCE PARAMETERS

5.1 Introduction

Various parameters can be utilized to evaluate the performance of our proposed PCF-SPR sensor that will be discussed in the next chapter. The key performance parameter of an SPR-PCF is based on the CL that is encountered due to the light propagation through the core. The value of the CL varies depending on the altering values of the RI of the analyte. WS and wavelength resolution can be two defining parameters for the difference in CL pattern due to the variation of the RI of the analyte. Besides, the use of two plasmonic materials concurrently next to each other gives rise to two peaks in the CL pattern of the proposed sensor. In order to establish a relationship between two distinct resonant peaks at two particular wavelengths, a novel parameter DPSS has been proposed[63]. The interaction between the PCF and the analyte under the influence of plasmonic materials can be described by the permittivity model of the materials. One of the most commonly used means to represent fused-silica is Sellmier's equation. Similarly, the characteristics of the plasmonic materials can be described by using the Drude-Lorentz Model. In the proposed sensor, air has been used as a dielectric which has a permittivity close to 1.

5.2 Sellmeier's Equation

As the background material of SPR-PCF sensor, either glass or polymer can be utilized. However, silica has been used as the background material of our proposed sensor. Sellmeier's Equation gives the permittivity model of silica as follows:

$$n^2(\lambda) = 1 + \frac{B_1\lambda^2}{\lambda^2 - C_1} - \frac{B_2\lambda^2}{\lambda^2 - C_2} - \frac{B_3\lambda^2}{\lambda^2 - C_3} \quad 5.1$$

The Sellmeier coefficients are as follows:

Table 5.1 Sellmeier's Constants

Constants	Values
B1	0.696
B2	0.408
B3	0.897
C1	0.0047μm2

C2	0.014μm2
C3	97.934 μm2

5.3 Drude-Lorentz Model

The generalized Drude-Lorentz model describes permittivity in the complex frequency plane in a simple and physically meaningful manner. To appropriately express permittivity behavior, it employs a set of simple poles with complex weights[95]. To estimate the dielectric constant of gold, the Drude-Lorentz model can be given as:

$$\varepsilon_g = \varepsilon_\infty - \frac{\omega^2{}_D}{\omega(\omega + j\gamma_D)} - \frac{\Delta\varepsilon\Omega^2{}_L}{(\omega^2 - \Omega^2{}_L) - J\Gamma_L\omega} \quad 5.2$$

Table 5.2 Drude-Lorentz Constants of Gold

Constants	Values
γ_D	31.84 πTHz
ε_∞	5.9673
ω_D	4227.24πHz
Γ_L/π	209.72 THz
Ω_L/π	1300.14 THz

The Drude-Lorentz model of GZO can be given as:

$$\varepsilon_{GZO} = \varepsilon_b - \frac{\omega^2{}_p}{\omega(\omega + j\gamma_p)} + \frac{f_1\omega^2{}_1}{(\omega^2{}_1 - \omega^2 - j\omega\gamma_1)} \quad 5.3$$

Table 5.3 Drude-Lorentz Constants of GZO

Constants	Values
ε_b	3.5402
ω_p	1.7473 eV
γ_p	0.04486 eV
f_1	0.5095
ω_1	4.2942 eV
γ_1	0.1017 eV

5.4 Wavelength Sensitivity

The wavelength sensitivity of a certain SPR-PCF is found by wavelength interrogation methods. Larger resonance wavelength variations with minimal changes in the RI of the unknown sample are signs of higher spectral sensitivity. It is calculated using the corresponding equation and the wavelength interrogation method:

$$S_\lambda = \Delta\lambda_{Peak} / \Delta n_a (nm / RIU) \quad 5.4$$

Here, $\Delta\lambda_{Peak} =$ Difference between two nearby wavelengths and $\Delta n_a =$ Neighboring refractive indices.

5.5 Wavelength Resolution

A RI sensor's sensor resolution parameter enables for the exact detection of even the smallest changes in a quantity.. A feature that helps determine the sensor's recognition precision is resolution. The wavelength resolution can be given as:

$$R(w) = \frac{\Delta\lambda_{\min}}{S_\lambda}(RIU) \quad 5.5$$

5.6 Double Peak Shift Sensitivity

In case of simultaneous use of two plasmonic materials, two resonant peaks occur in the CL curve. By broadening this idea of how peak-to-peak separation and analyte RI are related, a new sensitivity metric known as double peak shift sensitivities has been developed[63]. Differences in the refractive index (RI) have a significant impact on the sensor's capacity to switch between two peaks. The DPSS is given as:

$$S_{p-p} = \frac{\left(\lambda_{p2} - \lambda_{p1}\right)_{n_b} - \left(\lambda_{p2} - \lambda_{p1}\right)_{n_a}}{n_b - n_a} \times 10^3 (nm / RIU) \quad 5.6$$

$$S_{p-p} = \frac{\left(\lambda_{p2,n_b} - \lambda_{p2,n_a}\right) - \left(\lambda_{p1,n_b} - \lambda_{p1,n_a}\right)}{n_b - n_a} \times 10^3 (nm / RIU) \quad 5.7$$

The sample's refractive indices are represented by n_b and n_a. $\lambda_{p1, nb}$ and $\lambda_{p1, na}$, respectively denote elementary resonance wavelengths. Furthermore, $\lambda_{p2,nb}$ and $\lambda_{p2,na,}$ respectively, denote the auxiliary resonance wavelengths.

In order to solve electromagnetic equations in the earlier chapters, the material characterization equations mentioned in this chapter will be helpful. The performance of the sensor is evaluated by collecting confinement loss data for a range of wavelengths and refractive indices using metrics including waveguide sensitivity (WS), resolution, and double peak shift sensitivity (DPSS). The physical characteristics of the photonic crystal fiber (PCF), such as the airhole radius and plasmonic material thickness, are modified depending on the sensor's requirements. As a result, the features of the PCF can be modified and improved to fit the needs of the sensor. In the end, the use of the material characterization equations and fine-tuning of the physical characteristics of the PCF help to the thorough analysis and improvement of the sensor's performance.

CHAPTER 6

PROPOSED DESIGN: DUAL PEAK DOUBLE RESONANCE SENSING USING A DUAL PLASMONIC MATERIAL PCF-SPR SENSOR

6.1 Introduction

In this chapter, the structural details, optimization, and result analysis of a perfectly novel LSPR PCF sensor has been proffered. FEM in COMSOL Multiphysics v5.6 has been used for numerical analysis and structural design of the sensor. In the proposed sensor, external sensing has been used with the sample layer being situated outside the cladding region. The plasmonic layers have been placed just right under the layer of analytes using a particular arrangement. A GZO layer of thickness 10 nm has been chosen its low cost and extensive doping range. Besides, a gold layer of thickness 60 nm has been selected because of its chemical stability. The simultaneous placement of the plasmonic materials next to each other instead of sandwiching has enabled the creation of two separate peaks at two particular wavelengths while increasing the range of sensing of the sensor. After optimization of the design parameters for x-polarization, it has been found that the sensor exhibits a maximum DPSS value of 11,720 um/RIU which signifies its ability of shifting the double peaks for a slight change of RI of the analytes. Proper scrutiny of the simulation results also displayed a maximum WS value of 11,480 nm/RIU for analyte detection in the range of 1.39-1.40, extremely low CL values, and a minimum wavelength resolution value of 8.71×10^{-6} RIU. The range of sensing of the proffered sensor is observed to be 1.30 to 1.40, which covers the detection of myriad biochemical agents and solutions, such as, 10% glucose solution (RI=1.3477), 20% glucose solution (RI=1.3635), ethanol (RI=1.361)[96], RBC (RI=1.40), haemoglobin (RI=1.38), WBC (RI=1.36), plasma of blood (RI=1.35), acetone (RI=1.36), human liver (RI=1.369), mucosa of intestines of humans (RI=1.329-1.338), and so on[97], [98]. Additionally, the wide wavelength range of the sensor from 0.3 and 0.98 μm makes it eligible for both ultra-violet and visible spectrum applications. Therefore, the efficiency and usefulness of the sensor in the detection of the aforementioned biochemical substances covering a wide RI range need no mention.

6.2 Structural Design and Theoretical Modelling

The 2D cross-sectional view of our proffered sensor has been illustrated in the Figure 6.1 (a). The area of cladding of the sensor consists of two rings of circular air holes with hexagonal core. The large and small air hole radii have been denoted as r1 and r2 respectively. The optimal values of the large and small air holes have been found as 0.75 µm and 0.25 µm respectively. The purpose of the large air holes is to confine light towards the core while reducing the CL, whereas the small air holes have been placed with a view to ensuring sufficient energy transfer from the core to the plasmonic materials, and thus contributing to the formation of the SPP mode. The presence of only circular air holes contributes to the ease of the fabrication system[38]. The fabrication can be materialized via the standard stack-and-draw approach or by drilling during the preform stage. Stacked preforms for the sensor manufacture have been provided in Figure 6.1 (b). A Perfectly Matched Layer (PML) has been used for computational purpose as a mathematical boundary and serves the purpose of absorbing any emitted energy. Thickness of the PML is decided according to the dielectric thickness for the purpose of simulation and has no effect on the overall sensing system[99].

Gold has been used as a plasmonic material because of its chemical stability and negligible reactive property[50]. The optimized gold layer thickness has been found to be 60 nm. Whereas, GZO has been chosen because of its inexpensive and wide doping range[100]. The optimized GZO layer thickness has been chosen to be 10 nm. The optimization of plasmonic layer thickness was conducted for achieving a maximal value of DPSS. The properties of gold and GZO can be analyzed from the equations 6.2 and 6.3 respectively. Besides, as the material in background in the cladding region, fused silica has been used whose properties can be analyzed using the equation 6.1.

$$n^2(\lambda) = 1 + \frac{B_1\lambda^2}{\lambda^2 - C_1} - \frac{B_2\lambda^2}{\lambda^2 - C_2} - \frac{B_3\lambda^2}{\lambda^2 - C_3} \qquad 6.1$$

$$\varepsilon_g = \varepsilon_\infty - \frac{\omega^2{}_D}{\omega(\omega + j\gamma_D)} - \frac{\Delta\varepsilon\Omega^2{}_L}{(\omega^2 - \Omega^2{}_L) - J\Gamma_L\omega} \qquad 6.2$$

$$\varepsilon_{GZO} = \varepsilon_b - \frac{\omega^2{}_p}{\omega(\omega + j\gamma_p)} + \frac{f_1\omega^2{}_1}{(\omega^2{}_1 - \omega^2 - j\omega\gamma_1)} \qquad 6.3$$

A detailed explanation of the optimization of the thickness of plasmonic materials and radii of the air holes has been provided in later in this chapter.

Moreover, external sensing has been utilized for the purpose of analyte detection in the proffered sensor. The simultaneous placement of the two plasmonic materials has been made just beneath the analyte layer and next to each other; such a placement provides the basis for the formation of peaks at two concrete wavelengths in both the ultra-violet and visible spectrum range. Therefore, the working range of the sensor has been significantly enlarged.

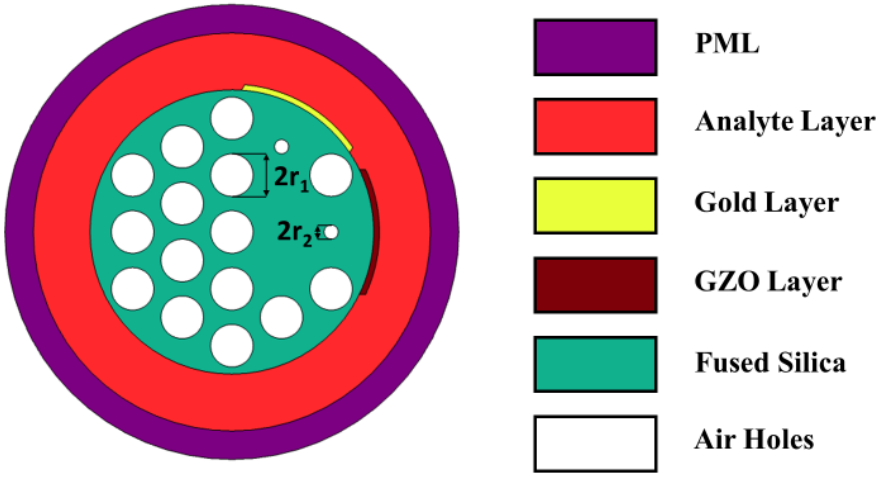

(a)

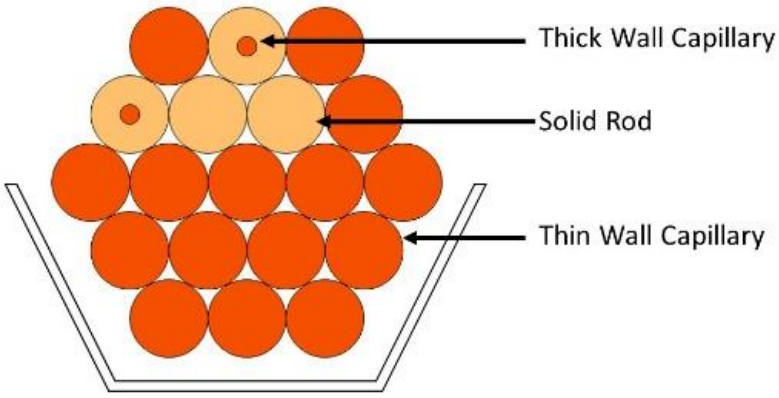

(b)

Fig 6.1 (a) 2D Schematic of the Proposed Sensor (b) Stacked Preform

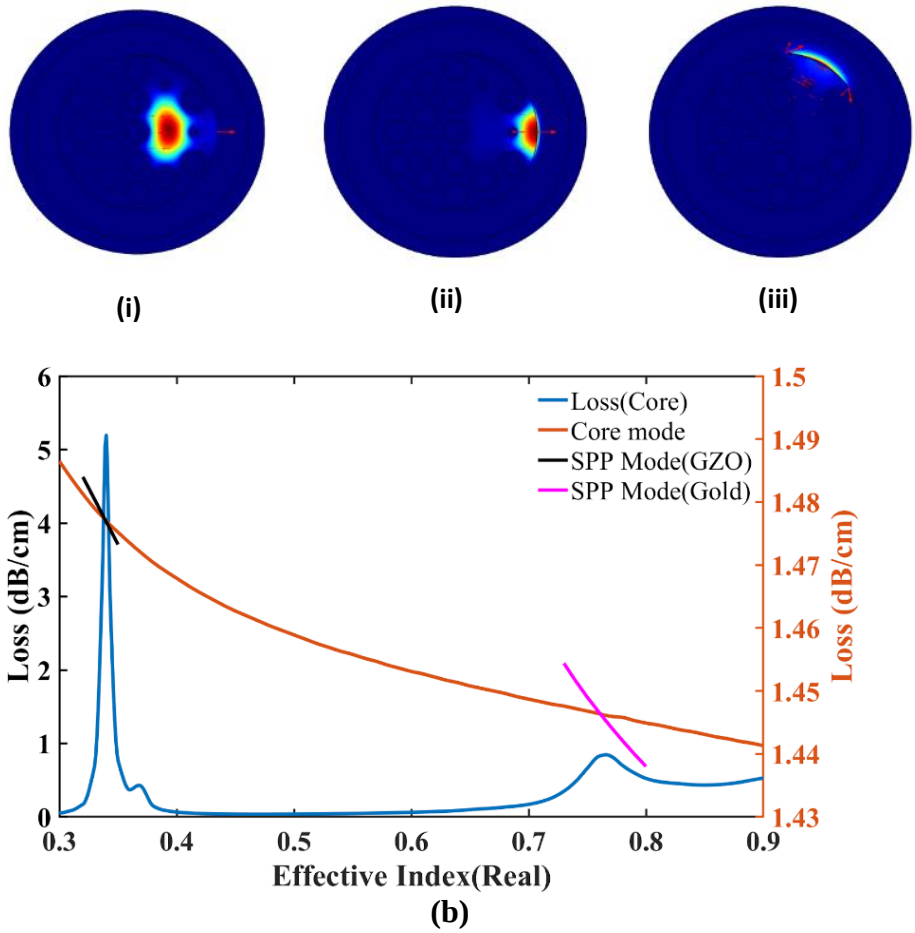

Fig 6.2 (a) Core mode (i) and SPP modes for Gold (ii) and (iii) GZO for an analyte RI = 1.38 (b) Dispersion relation between core mode and SPP modes for an RI=1.38

6.3 Sensor Performance Investigation and Optimization of different Geometrical Parameters

6.3.1 Guiding Properties and Dispersion Characteristics

In figure 6.2 (a), (i) denotes the optical field distribution for the core mode while (ii) and (iii) denote the SPP modes for gold and GZO respectively for x-polarization of an analyte of RI=1.38. Due to the presence of adequate number of large air holes, sufficient light has been confined inside the core and the figure 6.2 (a) (i) serves as its proof while it displays a strong confinement of the core mode.

Besides, due to the presence of the two small air holes, electromagnetic field partially reaches the cladding region from the core while the evanescence interacts with the plasmonic materials of the PCF-SPR sensors and excites the electrons on the surface. Resonance between the frequency of the surface electrons and the frequency of the evanescent field gives rise to surface

plasmon waves that travels through the metal-dielectric interface. The real parts of the effective mode index, η_{eff} for the core and the SPP modes match under the condition of resonance. A maximum transfer of energy also occurs from the core mode to the SPP during this resonant condition.

From figure 6.2 (b), it is evident that for an RI of 1.38, phase matching occurs, and two separate peaks are observed at two discrete wavelengths of 0.33973 μm and 0.76488 μm respectively. This has occurred due to the concurrent placement of the two plasmonic materials next to each other. Therefore, a double resonance phenomenon has evolved while providing the potential of working in the ultra-violet and visible spectrum range to the proffered sensor.

From Figure 6.3, we can observe that, the proposed sensor exhibits extremely low CL values in the RI range of 1.30 to 1.40. Resonance occurs due to phase matching conditions of the core mode and SPP mode at two concrete wavelengths. These wavelengths incur a red shift (right shift[101]) for increase in RI whereas, they undergo a blue shift (left shift[101]) for an RI decrease. The magnitude of shift for the first peak is smaller compared to that of the second peak. But it ultimately confirms the sensor's workability in the UV range. Furthermore, the CL values increase with the increase of RI. Therefore, the variation of the CL and the resonant wavelengths of the peaks can help the sensor detect slight changes in the RI of the analytes. For the first peak, the lowest and highest CL values have been observed to be 2.4971 dB/cm and 7.14067 dB/cm for RI=1.30 and 1.40 respectively.

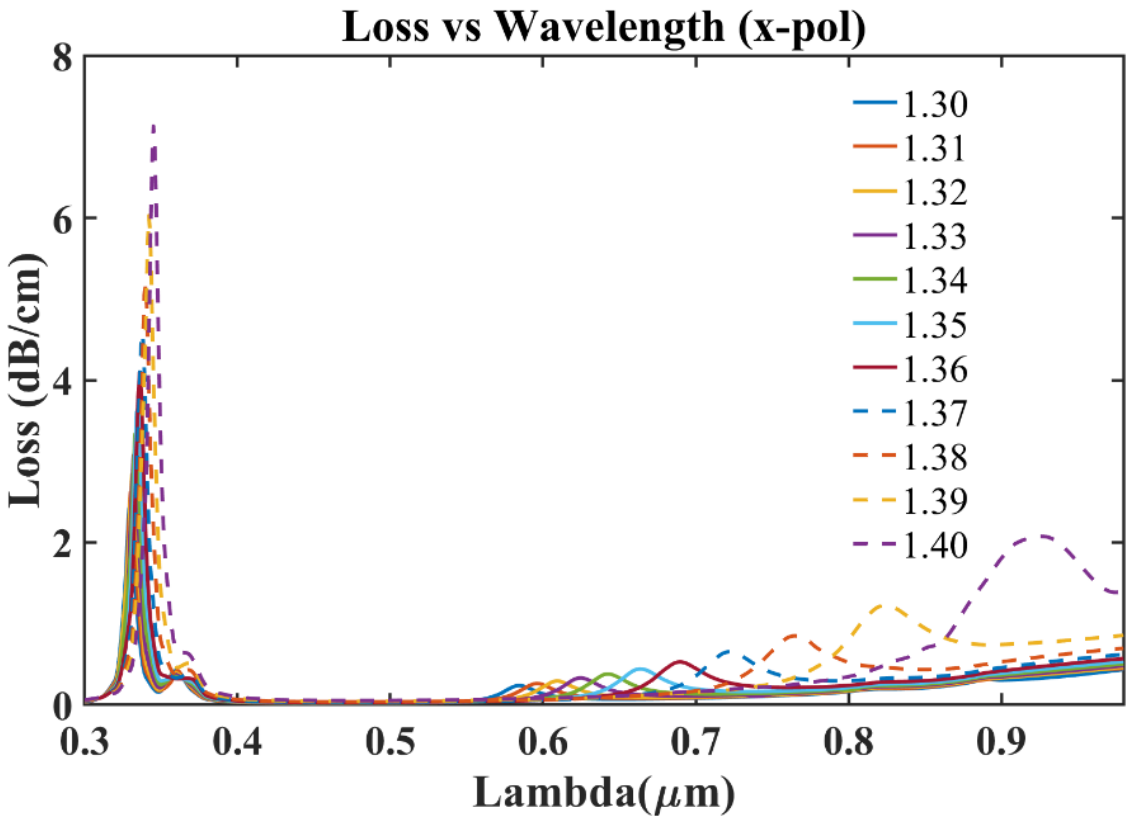

Fig 6.3 Analysis of the variation of the resonant wavelengths and

Moreover, the presented sensor has demonstrated a maximum Wavelength Sensitivity (WS) value of 11,480 nm/RIU in x-polarization because of fluctuation of RI from 1.39 to 1.4. A greater value of WS indicates a larger resonant wavelength shift due to the change in the value of RI. Equation 6.4 has been presented to calculate the value of WS for the sensor.

$$s_{\lambda} = \Delta\lambda_{Peak} / \Delta n_a (nm / RIU) \qquad 6.4$$

Furthermore, from equation 6.5, the minimal value of the sensor's wavelength resolution has been calculated to be 8.71×10^{-6}. Wavelength interrogation technique has been utilized to examine the sensor resolution in this case. The minimal value of wavelength resolution of the sensor in the order of 10^{-6} establishes the fact that the sensor is capable of detecting RIs in the extremely minute range of 10^{-6}. Therefore, the enhanced detecting capability of the sensor can be realized through this.

$$R(w) = \frac{\Delta\lambda_{\min}}{s_{\lambda}}(RIU) \quad 6.5$$

Moreover, the sensor's performance in terms of DPSS was improvised by optimizing the geometric parameters used in the sensor design. For the proposed sensor, the gold layer thickness, the GZO layer thickness, the small air hole radius, and the large air hole radius were optimized with a view to achieving the maximal DPSS value. The optimization of the parameters has been described in detail later in this chapter along with necessary graphs acquired from simulations.

6.3.2 Optimal Sensor Calibration and Diverse Expansion of Sensor Length

From the figure 6.4, the linearity properties of the first and the second peaks in terms of the change of resonant wavelength with the change of RI have been observed. Regression analysis was used to validate the sensor's linearity. After observing the resonant wavelength values for a number of RIs and through adjustment of several settings, a conclusion that can be derived is that the equation 6.1 with the co-efficient of determination, R^2 value of 0.9549 epitomized the first peak according to linear regression, whereas, according to quadratic fitting, equation 6.2 R^2 value of 0.9963 that is much closer 1 represents the first peak. Moreover, for the representation of the second peak, equation 6.3 and 6.4 derived according to linear regression and polynomial fitting respectively with R^2 values of 0.9324 and 0.9947 respectively. Therefore, both the peaks can be more concisely estimated using the concept of quadratic fitting.

$$y = 0.1333 + 0.1555x \quad 6.6$$

$$y = 1.0985 - 2.8216x + 2.1417x^2 \quad 6.7$$

$$y = 25.6061 - 66.3748x + 43.6032x^2 \quad 6.8$$

$$y = 2.5055 - 2.6976x \quad 6.9$$

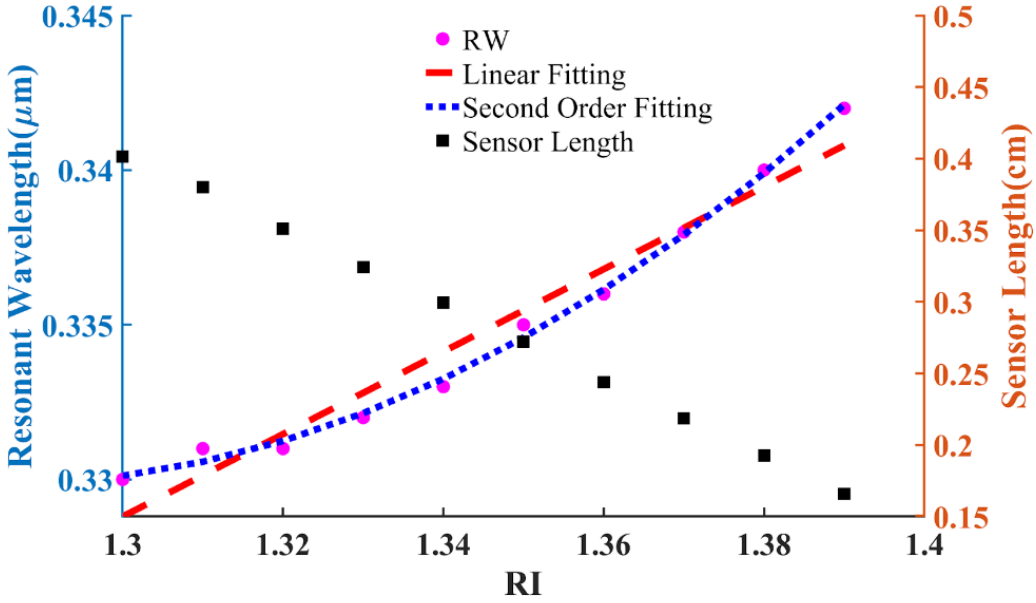

(a)

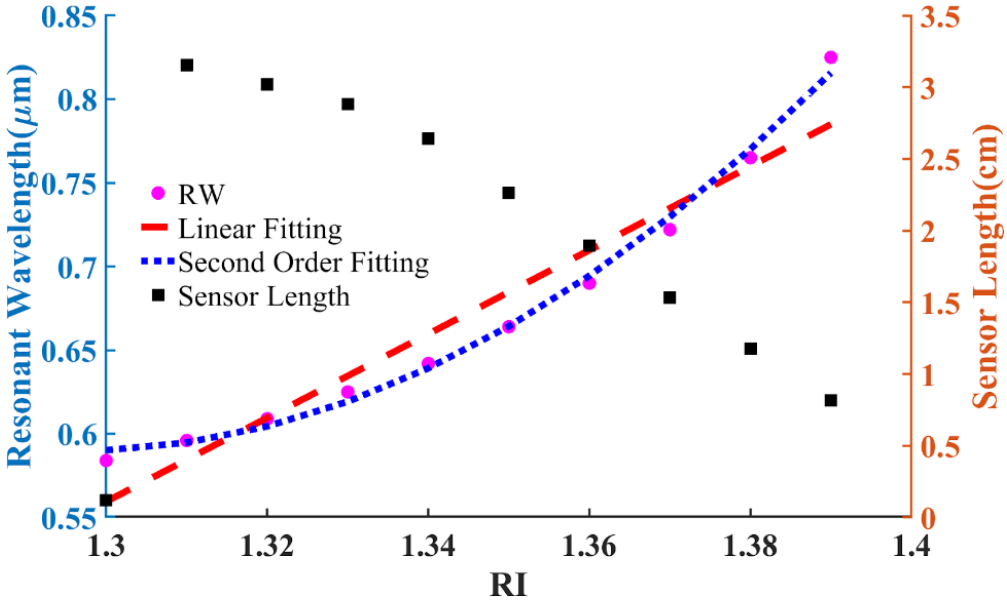

(b)

Fig 6.4 Regression analysis for the resonance wavelength for the change of RI in case of first peak (a) and second peak (b)

Moreover, figure 7.4 also states the permissible length of sensor for accommodating the first and second peak's CL values. While taking both the peaks into consideration, it can be

concluded that the sensor length has to be up to the maximum value of 3.149 cm but not less than 0.8169 cm. It is to mention that an inversely proportional relationship exists between the CL value and the length of the senor. Therefore, the negligible CL values of the sensor contributes to the expansion of the sensor length[1].

6.3.3 Optimization of GZO Layer Thickness

From the figure 6.5 (a), the effect of the GZO layer thickness's variation on the CL and DPPS value can be contemplated. It can be observed that for an RI shift from 1.37 to 1.38, the resonant wavelengths for the dual peaks incurred a shift along with the change in the thickness of the GZO layer. Therefore, the DPSS values also experienced a change. Initially, the GZO layer thickness was taken to be 30 nm while keeping all other parameter values fixed. The DPSS value was found to be 2300 $nmRIU^{-1}$ for GZO layer thickness=30 nm and all the other parameters retaining their initial conditions. As we decreased the GZO layer thickness value, the DPSS experienced a rise. The maximum value of DPSS was obtained to be 4288 $nmRIU^{-1}$ for a thickness of GZO layer of 10 nm and the value significantly decreased to 1627 nm/RIU and 4236 nm/RIU for the GZO layer thickness of 15 nm and 5 nm respectively. Therefore, 10 nm was the optimal GZO layer thickness value providing the greatest shift of the double peaks for a slight variation in the RI value.

6.3.4 Optimization of Gold Layer Thickness

From the figure 6.5 (b), for an RI variation of 1.37 to 1.38, it depicts that alteration was done from the range of 30 nm to 70 nm of the gold layer thickness The DPSS rose from 4032 nm/RIU to 4288 nm/RIU by increasing the gold layer thickness from 55 to 60 nm while keeping the GZO layer thickness constant at 10 nm. As the gold layer width was extended from 60 to 65 nm, the DPSS decreased, indicating that 60 nm is the optimal gold layer thickness. The value of DPSS increased due to an increase in the displacement of the two peaks caused by RI fluctuation.

6.3.5 Optimization of Air Hole Radii

As shown in figure 6.5 (c), the radius of the large air holes, r1 was increased from 0.7 µm to 0.8 µm. The DPSS value drastically increased to 4288 nm/RIU when r1 value was taken to be 0.75 µm. However, it incurred a decrease to 4150 nm/RIU and 4031 nm/RIU when r1 value

was taken to be 0.80 µm and 0.7 µm respectively. Throughout this observation, the GZO and gold layer thickness values were 10 nm and 60 nm respectively. So, the optimized r1 value was 0.75 µm. So, when the RI of the analyte is slightly altered, the highest value of DPSS implies the highest shift of two peaks for r1=0.75 µm. Since smaller air holes indicate that light will be derailed more from the centre towards the plasmonic materials, we can observe that the CL value decreased with the increase in the r1 value[60]. Furthermore, in figure 6.5 (d), the small air holes' radius, r2, was extended from 0.20 µm to 0.30 µm where the DPSS value significantly increased from 4051 nm/RIU to 4288 nm/RIU when the value of r2 was increased from 0.2 µm to 0.25 µm, and it deteriorated to 4125 nm/RIU when the value of r2 was increased to 0.30 um. Therefore, r2=0.25 µm was taken to be the optimized value because it had the largest peak shift and DPSS value. It is to mention that with an increase in the value of the size of the small air holes, the CL values decreased.

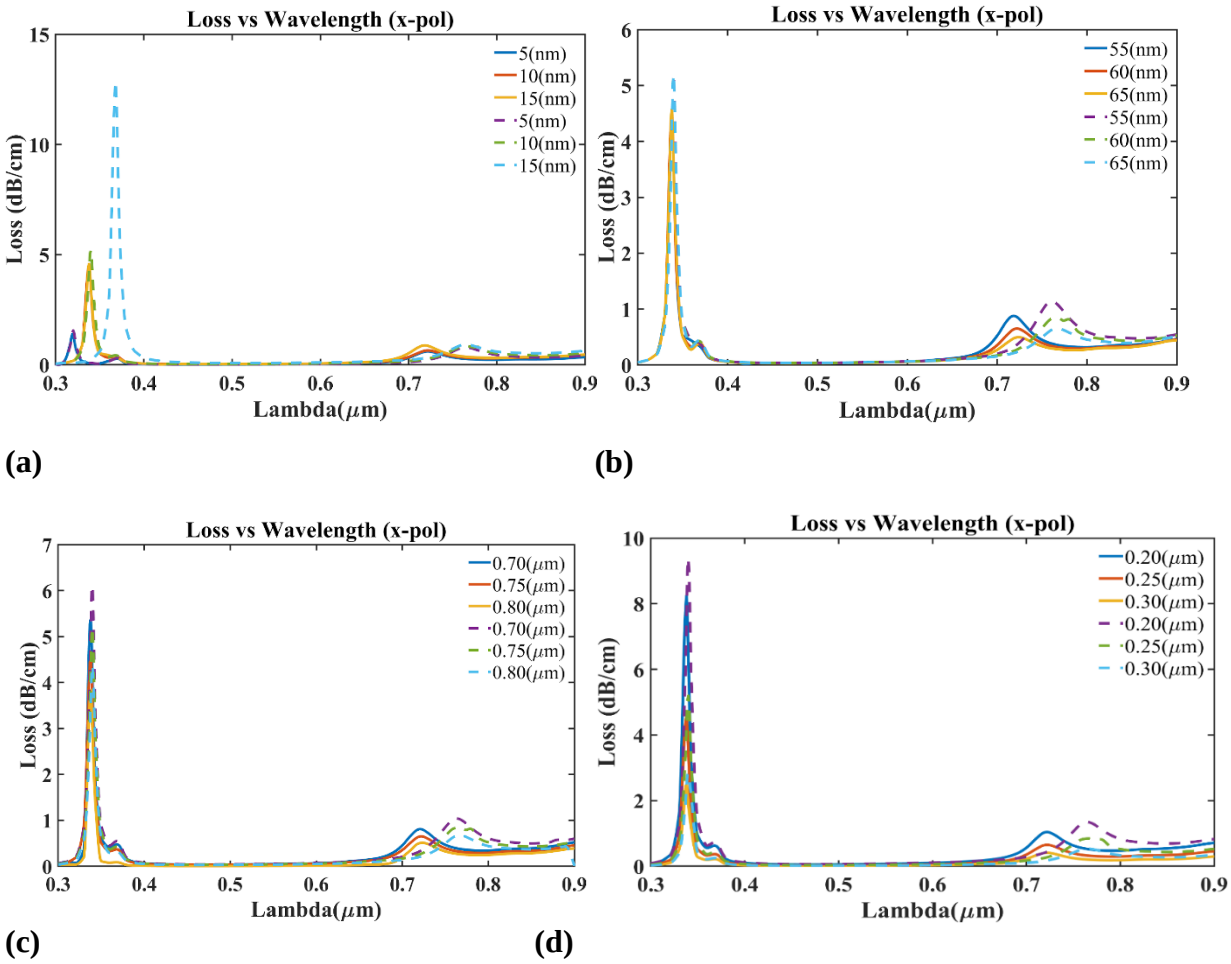

Fig 6.5 (a) For analytes with RI of 1.37 and 1.38, confinement loss fluctuation with changing (a) GZO layer thickness, (b) Gold layer thickness, and (c) Large air hole radii (d) Small air hole radii

6.3.5 Double Resonance and Double Peak Shift Sensitivity

SPR phenomenon is the result of the matching of the frequency of the evanescent field and the surface electrons of the plasmonic materials. Therefore, maximum energy is transferred from the core mode to the SPP mode as their refractive indices match, while producing a unique CL peak due to the resonance phenomenon. However, in the case of the proffered sensor, the evanescent field splits causing the evolution of two separate SPP modes at two distinct wavelengths in x-polarization. The first peak in the ultra-violet region is introduced by GZO and the second peak in the visible spectrum range arises due to the use of gold. As the RI value for x-pol rises from 1.30 to 1.38, the DPSS value climbs from 1050 nm/RIU to 5769 nm/RIU, which indicates a high shift of the double peaks of the sensor due to RI alteration. From figure 6.5(d), it can be realized that for an analyte with RI of 1.38 in x-polarization, the largest loss peaks of 5.2079 dB/cm and 0.8453 dB/cm were obtained at wavelengths of 0.33991 m and 0.76691 m, respectively. These loss peaks show the link between spread of light in the core guided mode and SPP modes. The DPSS value for the sensor has been calculated using the equation 6.10 or 6.11. The effect of the variation of RI on the DPSS value can be contemplated from figure 6.6.

$$S_{p-p} = \frac{\left(\lambda_{p2} - \lambda_{p1}\right)_{n_b} - \left(\lambda_{p2} - \lambda_{p1}\right)_{n_a}}{n_b - n_a} \times 10^3 (nm / RIU) \qquad 6.10$$

$$S_{p-p} = \frac{\left(\lambda_{p2,n_b} - \lambda_{p2,n_a}\right) - \left(\lambda_{p1,n_b} - \lambda_{p1,n_a}\right)}{n_b - n_a} \times 10^3 \left(nm / RIU\right) \qquad 6.11$$

Therefore, the high double peak shift of the proposed sensor proves the extensive potential of our sensor in the field of biosensing as the double peaks are highly sensitive to the change of RI value.

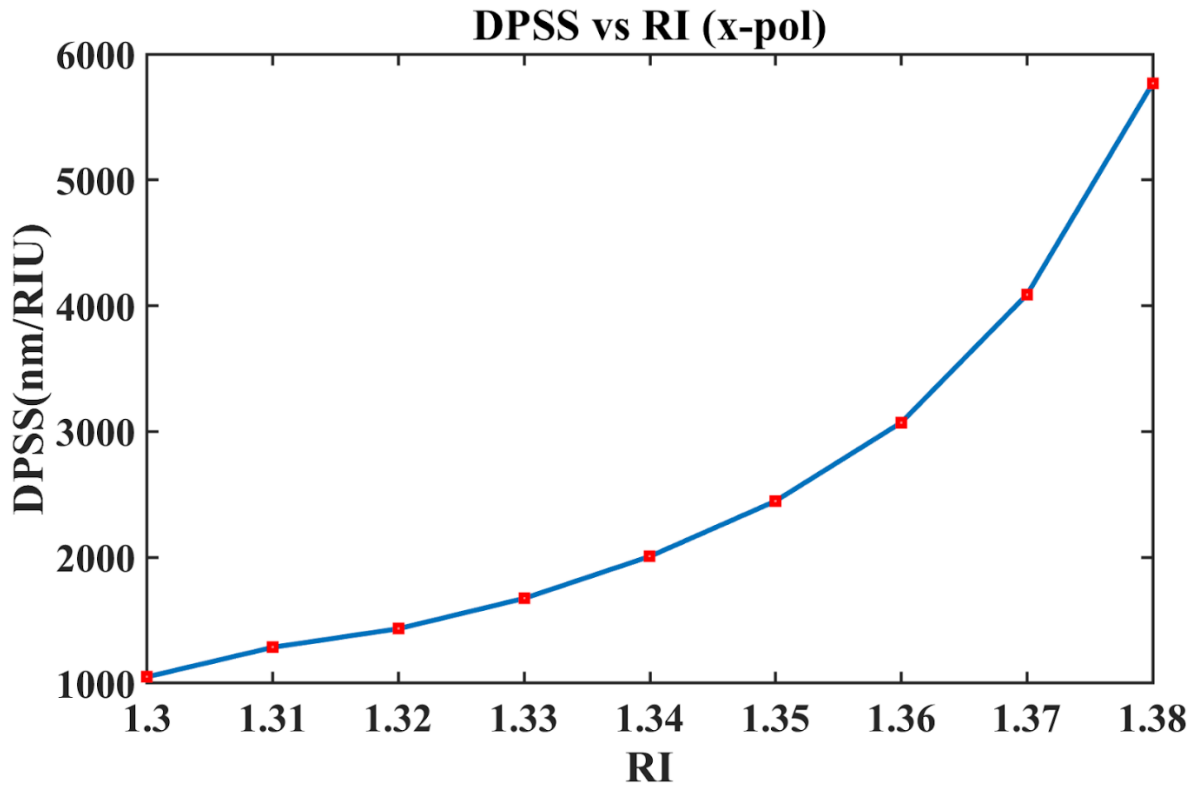

Fig 6.6 Analysis of the variation of the value of DPSS for the alteration of RI values

6.3.5 Wide Range of Detection of RI

The proposed novel sensor is capable of detecting analytes in the wide range of RI from 1.30 to 1.40, while ensuring its workability in both the ultra-violet and visible spectrum range. Figure 8.2 displays the effect of the variation of the resonant wavelength and CL values with the alteration of RI values. The CL peaks incur a shift to the right due to RI increase, whereas they incur a left shift for RI decrease. Moreover, the negligible CL values ensure the sensor's appropriateness for applications requiring large sensor lengths[1]. The CL value for the sensor can be calculated using the equation 6.12

$$\alpha(dB/cm) = 8.686 \times \left(\frac{2\pi}{\lambda}\right) \times \mathrm{Im}(n_{eff}) \times 10^4 \qquad 6.12$$

It is noteworthy that as propagation factors decline, the core and SPP modes often merge at longer wavelengths, allowing the effective mode index to decline along with the RI increase. Moreover, the RI value of the analyte will eventually reach that of the cladding region covered in fused-silica[102].

6.4 Performance Comparison of the Proffered Sensor with the Previous Works

Table 6.1 Comparison With Previous Studies

Ref	RI Range	WS_{max} (nm/RIU)	Wavelength Resolution (RIU)	Double peak sensitivity (nm/RIU)
[103]	1.33-1.38	4600	2.17×10^{-5}	---
[104]	1.33-1.40	9000	1.11×10^{-5}	---
[105]	1.34-1.37	9000	1.11×10^{-5}	---
[106]	1.33-1.45	5300	---	---
[107]	1.35-1.40	10000	2×10^{-5}	---
[108]	1.32-1.34	5000	2×10^{-5}	---
This work	1.30-1.4	11480	8.71×10^{-3}	11,720

From table 6.1, it can be contemplated that the sensor displays an enhanced WS of 11,480 nm/ RIU in the visible spectrum range, with a corresponding wavelength resolution of 8.71×10^{-6}. As a result, the proposed sensor performs better in terms of wavelength sensitivity and can detect analytes more concisely than the major portion of the works stated in the literature.

CHAPTER 7

FABRICATION OF THE SENSOR

7.1 Introduction

The effectiveness of an LSPR sensor extensively depends upon the feasibility of its fabrication. Therefore, we aim to design the proffered sensor with the least amount of fabrication difficulties possible. Sensors with a difficult manufacturing process should not be prioritized over optical fiber designs with better developed sensing activities and simpler fabrication techniques. Moreover, the ease of fabrication process also contributes to ensuring the cost-effectiveness of the sensors. It is to mention that the use of circular air holes in the cladding region helps in reducing the fabrication difficulties of the sensors[38]. The proffered sensor with the desired core structure is fabricated utilizing the Stack and Draw Method after which Chemical Vapor Deposition Technique is used to give the metal layer coating. The fabrication technique and the fabrication tolerance of the proffered sensor has been discussed in detail later in this chapter.

7.2 Fabrication Method

The stacked preform of the proposed sensor has been presented in figure 6.1 (b). Since hexagonal shaped cores are more fabrication friendly and easy to implement, the rods are arranged in a hexagonal manner, rather than being arranged in D-shape since D-shaped cores are more complex and less symmetric. The capillaries and solid rods will be placed according to the airhole configuration. Depending on the level of confinement needed at the core, the solid rods were chosen. At first, thick-walled capillaries will be chosen 100 times larger than their actual size and these thick-walled capillaries contribute to the transfer of energy from the core to the plasmonic materials. Furthermore, the number of thin-walled capillaries are chosen with a view to ensuring low CL value and increased sensitivity. After that, the cane intermediate preform will be drawn till the suggested measurement accuracies are achieved.

Next, a photolithography process consisting of two steps will be implemented for the purpose of creating the gold and GZO layer coatings[109]. The metal layer will first be deposited to the

fiber surface utilizing the chemical vapor deposition (CVD) technique[110]. The remaining area will then be etched while the targeted region is masked. This process will be followed at first for gold and when the gold layer will be obtained, the GZO layer will be obtained following the same procedures. The selected regions comprising the necessary GZO and gold layers will then be masked off once again before the remaining regions are subjected to etching. It is to mention that the sensor layer will be implemented using two pumps, one of them will be for introducing analyte and another one for evacuation[102]. Therefore, the fabrication of the sensor we have proffered is possible by implementing the aforementioned steps. The steps of the fabrication of the sensor have been portrayed in detail in the figure 7.1.

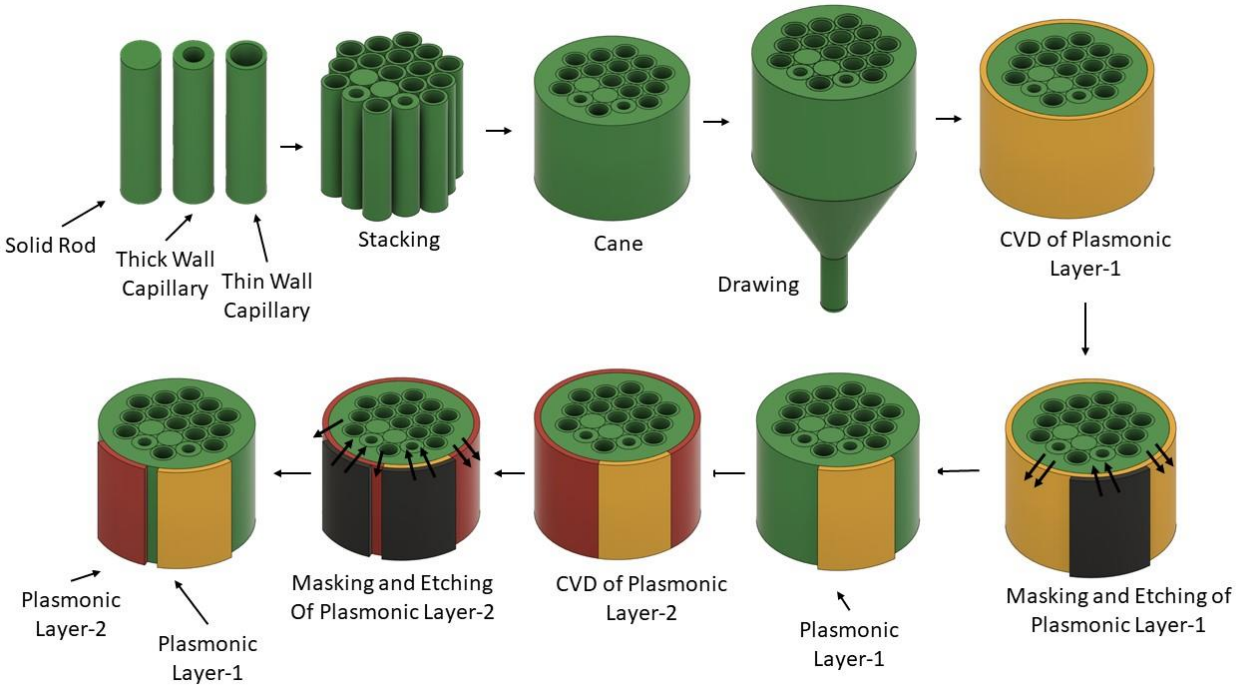

Fig 7.1 Fabrication steps of the proffered sensor

7.3 Fabrication Tolerance

It is mentionable that 1% to 2% disparity from the ideal structural dimensions can be observed since fabrication techniques cannot always ensure precise dimensions during the manufacturing procedure[110]. Therefore, the r1 and r2 values were varied from their original values by 5 % and 10 % with a view to investigate the permission of a wide range of fabrication errors. From figure 7.2, it can be observed that as r1 radius was increased by 5% and 10% from the ideal value, the confinement loss dropped from the actual value. Furthermore, the CL value increased for decreasing the r1 value by 5 % and 10 % from its optimal value. The confinement

loss for the first peak was 5.86674 $dBcm^{-1}$ and 6.50708 $dBcm^{-1}$, respectively, for 5% and 10% reductions in the value of r1. When the r1 value increased by 5% or 10%, respectively, it changed to 4.56206 $dBcm^{-1}$ and 3.96734 $dBcm^{-1}$. For the second peak, the confinement loss was 0.97784 $dBcm^{-1}$ and 1.14688 $dBcm^{-1}$ for 5% and 10% decreases in r1 value, respectively. For 5% and 10% increases in r1, it changed to 0.70801 $dBcm^{-1}$ and 0.46687 $dBcm^{-1}$ respectively.

Although the first peak shifted from its ideal position when the r1 value increased and decreased by 5 percent and 10 percent, respectively, it stayed permanently at a certain resonant wavelength. When the value of r1 was reduced by 5% or 10%, the resonant wavelength for the second peak moved away from its ideal location. But it stayed fixed at a particular wavelength for r1 value increase by 5 percent and10 percent.

Furthermore, it can be realized from figure 7.3 that when the r2 value was altered by 5% and 10%, the first peak shifted from its ideal position but stayed permanently at a certain resonant wavelength. The resonant wavelength for the second peak also changed from its ideal location but stayed stable at a specific wavelength for r2 values of 5% and 10% decrease and increase, respectively. The confinement loss for the first peak changed to 6.02742 $dBcm^{-1}$ and 6.98779 $dBcm^{-1}$ for 5% and 10% decreases in r2 values, respectively. For a 5% and 10% rise in r2 value, respectively, it changed to 4.46960 $dBcm^{-1}$ and 3.84101 $dBcm^{-}1$. The confinement loss was 0.92750 $dBcm^{-1}$ and 1.04239 $dBcm^{-1}$, respectively, for increases in r2 by 5% and 10%, respectively. For a 5% and 10% decrease in r2 value, it changed to 0.73755 $dBcm^{-1}$ and 0.65832 $dBcm^{-1}$ respectively.

It can be concluded that although the proffered sensor exhibits variation in CL amplitude due to the deviation of the r1 and r2 from their optimal values, very negligible deviation of peaks from their actual position is observed. Therefore, the tolerance of the sensor against fabrication errors of 5 % and 10 % can be confirmed.

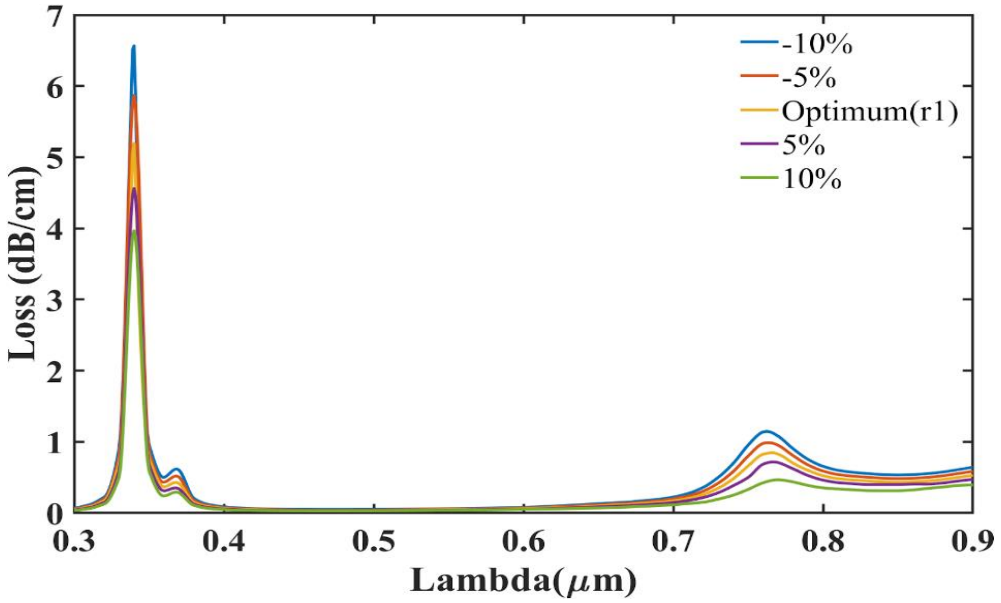

Fig 7.2 Confinement loss spectrum at RI 1.38 of the analyte for r1 variations of ±5% and ±10%

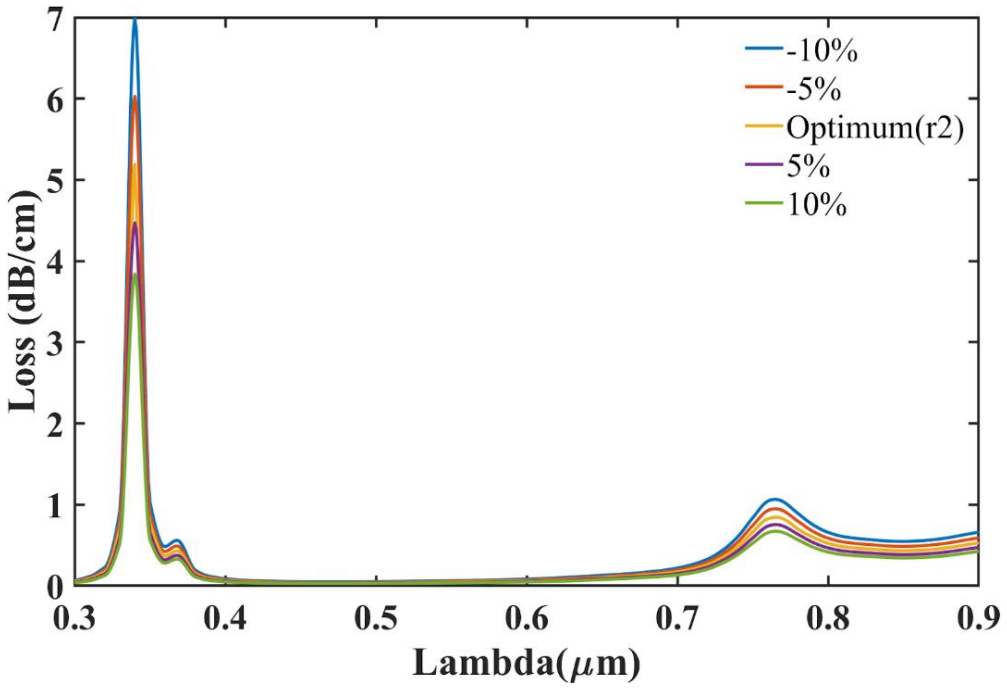

Fig 7.3 Confinement loss spectrum at RI 1.38 of the analyte for r2 variations of ±5% and ±10%

CHAPTER 8

8.1 FUTURE WORKS AND SOCIO-CULTURAL IMPACTS

8.1.1 Socio-Cultural Impacts of LSPR Sensors

PCF-LSPR sensors can significantly contribute to the bio-sensing field with a view to developing the agricultural, medical, and environmental sectors. The contribution of the LSPR sensors in the aforementioned domains have been narrated in brief below:

- LSPR sensors have been successfully utilized in the in the detection of DNA-hybridization[111].
- LSPR sensors have also shown potentials in the real-time monitoring of insulin, and detection of ultra-sensitive influenza and HIV-1 virus [112][113][114].
- LSPR provides improved sensitivity and limits of detection (LOD) for the detection of calcium, iron, copper, sodium, potassium, cobalt, manganese, and molybdenum using laser-induced breakdown spectroscopy (LIBS)[115].
- Besides, LSPR can also be used for the detection of Organophosphate (OP) pesticides which pose a great threat to human health[116].
- LSPR sensors can prove to be effective in the nano scale detection of deadly viruses[117].
- Mercury detection is also possible using LSPR by observing the affinity difference between Hg and Au nanoparticles with DNA which causes greater LSPR intensities[118].

Therefore, LSPR sensors demonstrate myriad characteristics that can be termed as the epitome of its efficacy in the biomedical, environmental and agricultural domains.

8.1.2 Future Works

In the near future, we hope to put endeavours towards the development of our proposed sensor. The scopes of future works which our proffered sensor exhibits are mentioned as follows:

- Implementation of realistic 3D model of the sensor
- Improving the sensor's Amplitude Sensitivity and Wavelength Sensitivity
- Implementation of different materials and tune parameters on the sensor structure
- Expanding the application areas of the sensor
- Experimentation of the sensor properties by varying the number and position of small and large air holes in the cladding region

8.2 CONCLUSION

In this thesis, we have proposed the implementation of an LSPR based PCF biosensors that is capable of detecting analytes in the wide range of RI from 1.30 to 1.40. All our simulations have been performed using FEM in COMSOL Multiphysics v5.6 using fine meshing. As we have used two plasmonic materials, gold and GZO, side by side, our sensor exhibited a significantly broad working range both in the ultra-violet and visible light spectrum. This eventually caused the splitting of the evanescent field and gave rise to two distinct peaks at two separate wavelengths. Moreover, we have introduced a novel parameter, DPSS that efficiently measures the displacement of the dual peaks for the variation of the analytes' RI. Our sensor consisted of both a hexagonal core and circular air holes in the cladding region which result in ease of fabrication. Moreover, we have optimized the design parameters of our sensos based on the maximum value of DPSS which was never done in any of the literatures that we have cited. At optimal design conditions, our sensor demonstrated a highest DPSS value of 11,720 $umRIU^{-1}$ for x-pol which depicts that a small variation in analytes' RI is related with a higher wavelength displacement for both the peaks. Furthermore, due to its extremely low CL, the sensor is appropriate for applications requiring longer sensor lengths. Therefore, it can be realized that using gold and GZO at the same time can produce strong sensing qualities and has expanded the spectrum of its uses in the fields of biomedical engineering and communication technology. In other words, we can arrive at the conclusion that a high DPSS value has increased the potentiality of the suggested sensor for a variety of functions in the UV and visible range and has significantly contributed in widening its application arena in myriad domains.

References

[1] M. R. Islam *et al.*, "Design of a dual spider-shaped surface plasmon resonance-based refractometric sensor with high amplitude sensitivity," *IET Optoelectron.*, vol. 17, no. 1, pp. 38–49, 2023, doi: 10.1049/ote2.12084.

[2] N. Bhalla, P. Jolly, N. Formisano, and P. Estrela, "Introduction to biosensors," *Essays Biochem.*, vol. 60, no. 1, p. 1, Jun. 2016, doi: 10.1042/EBC20150001.

[3] P. Skládal, "Piezoelectric biosensors," *TrAC - Trends Anal. Chem.*, vol. 79, pp. 127–133, May 2016, doi: 10.1016/j.trac.2015.12.009.

[4] P. Mehrotra, "Biosensors and their applications – A review," *J. Oral Biol. Craniofacial Res.*, vol. 6, no. 2, pp. 153–159, May 2016, doi: 10.1016/J.JOBCR.2015.12.002.

[5] C. Chen and J. Wang, "Optical biosensors: an exhaustive and comprehensive review," *Analyst*, vol. 145, no. 5, pp. 1605–1628, Mar. 2020, doi: 10.1039/C9AN01998G.

[6] Y. T. Chen *et al.*, "Review of Integrated Optical Biosensors for Point-of-Care Applications," *Biosens. 2020, Vol. 10, Page 209*, vol. 10, no. 12, p. 209, Dec. 2020, doi: 10.3390/BIOS10120209.

[7] C. Chen and J. Wang, "Optical biosensors: an exhaustive and comprehensive review," *Analyst*, vol. 145, no. 5, pp. 1605–1628, Mar. 2020, doi: 10.1039/C9AN01998G.

[8] A. Tereshchenko *et al.*, "Optical biosensors based on ZnO nanostructures: advantages and perspectives. A review," *Sensors Actuators B Chem.*, vol. 229, pp. 664–677, Jun. 2016, doi: 10.1016/J.SNB.2016.01.099.

[9] L. Stolz, "Chapter 29. The Use of Surface Plasmon Resonance Based Biosensors in Drug Discovery," *Annu. Rep. Med. Chem.*, vol. 33, no. C, pp. 293–299, 1998, doi: 10.1016/S0065-7743(08)61094-5.

[10] A. Syahir, K. Usui, K. Tomizaki, K. Kajikawa, and H. Mihara, "Label and Label-Free

Detection Techniques for Protein Microarrays," *Microarrays 2015, Vol. 4, Pages 228-244*, vol. 4, no. 2, pp. 228–244, Apr. 2015, doi: 10.3390/MICROARRAYS4020228.

[11] "Surface Plasmon Resonance (SPR): Label-Free Detection | Biochemistry | JoVE." https://www.jove.com/v/5697/surface-plasmon-resonance-spr (accessed May 27, 2023).

[12] X. Fan, "Sensitive surface plasmon resonance label-free biosensor on a fiber end-facet," *Light Sci. Appl. 2022 111*, vol. 11, no. 1, pp. 1–2, Nov. 2022, doi: 10.1038/s41377-022-01025-x.

[13] P. Zhang, G. Ma, W. Dong, Z. Wan, S. Wang, and N. Tao, "Plasmonic scattering imaging of single proteins and binding kinetics," *Nat. Methods 2020 1710*, vol. 17, no. 10, pp. 1010–1017, Sep. 2020, doi: 10.1038/s41592-020-0947-0.

[14] V. Sharif and H. Pakarzadeh, "High-performance surface plasmon resonance fiber sensor based on cylindrical vector modes," *Sci. Reports 2023 131*, vol. 13, no. 1, pp. 1–9, Mar. 2023, doi: 10.1038/s41598-023-31524-9.

[15] S. Singh, B. Chaudhary, A. Upadhyay, D. Sharma, N. Ayyanar, and S. A. Taya, "A review on various sensing prospects of SPR based photonic crystal fibers," *Photonics Nanostructures - Fundam. Appl.*, vol. 54, p. 101119, May 2023, doi: 10.1016/J.PHOTONICS.2023.101119.

[16] S. Mittal, T. Sharma, and M. Tiwari, "Surface plasmon resonance based photonic crystal fiber biosensors: A review," *Mater. Today Proc.*, vol. 43, pp. 3071–3074, Jan. 2021, doi: 10.1016/J.MATPR.2021.01.405.

[17] M. S. Islam *et al.*, "A novel Zeonex based photonic sensor for alcohol detection in beverages," *2nd IEEE Int. Conf. Telecommun. Photonics, ICTP 2017*, vol. 2017-Decem, pp. 114–118, 2018, doi: 10.1109/ICTP.2017.8285905.

[18] M. Aminul Islam, M. Rakibul Islam, M. Moinul Islam Khan, J. A. Chowdhury, F. Mehjabin, and M. Islam, "Highly Birefringent Slotted Core Photonic Crystal Fiber for THz Wave Propagation," *Phys. Wave Phenom.*, vol. 28, no. 1, pp. 58–67, 2020, doi: 10.3103/S1541308X20010021.

[19] R. H. Khan, A. A. Chowdhury, and M. R. Islam, "Wave-Shaped Microstructure Cancer Detection Sensor in Terahertz Band : applied sciences Wave-Shaped Microstructure

Cancer Detection Sensor in Terahertz Band : Design and Analysis," no. May, 2023, doi: 10.3390/app13095784.

[20] M. A. Al Mahmud, M. R. Islam, A. N. M. Iftekher, M. M. Rahman, and F. A. Mou, "Design and numerical analysis of a porous core photonic crystal fiber for refractometric THz sensing," *Microsyst. Technol.*, vol. 29, no. 1, pp. 115–126, 2023, doi: 10.1007/s00542-022-05396-4.

[21] M. M. Rahman, F. A. Mou, M. I. H. Bhuiyan, and M. R. Islam, "Refractometric THz Sensing of Blood Components in a Photonic Crystal Fiber Platform," *Brazilian J. Phys.*, vol. 52, no. 2, 2022, doi: 10.1007/s13538-022-01054-2.

[22] M. M. Rahman, F. A. Mou, M. I. H. Bhuiyan, M. A. Al Mahmud, and M. R. Islam, "Design and characterization of a photonic crystal fiber for improved THz wave propagation and analytes sensing," *Opt. Quantum Electron.*, vol. 54, no. 10, pp. 1–29, 2022, doi: 10.1007/s11082-022-04057-0.

[23] M. R. Islam *et al.*, "Design of a hexagonal outlined porous cladding with vacant core photonic crystal fibre biosensor for cyanide detection at THz regime," *IET Optoelectron.*, vol. 16, no. 4, pp. 160–173, 2022, doi: 10.1049/ote2.12067.

[24] M. R. H. Khan, F. A. M. Ali, and M. R. Islam, "THz sensing of CoViD-19 disinfecting products using photonic crystal fiber," *Sens. Bio-Sensing Res.*, vol. 33, p. 100447, 2021, doi: 10.1016/j.sbsr.2021.100447.

[25] M. A. Islam, M. R. Islam, S. Siraz, M. Rahman, M. S. Anzum, and F. Noor, "Wheel structured Zeonex-based photonic crystal fiber sensor in THz regime for sensing milk," *Appl. Phys. A Mater. Sci. Process.*, vol. 127, no. 5, May 2021, doi: 10.1007/s00339-021-04472-2.

[26] M. R. Islam, A. N. M. Iftekher, F. A. Mou, M. M. Rahman, and M. I. H. Bhuiyan, "Design of a Topas-based ultrahigh-sensitive PCF biosensor for blood component detection," *Appl. Phys. A Mater. Sci. Process.*, vol. 127, no. 2, Feb. 2021, doi: 10.1007/S00339-020-04261-3.

[27] M. A. Islam, M. R. Islam, A. M. Al Naser, F. Anzum, and F. Z. Jaba, "Square structured photonic crystal fiber based THz sensor design for human body protein detection," *J. Comput. Electron.*, vol. 20, no. 1, pp. 377–386, 2021, doi: 10.1007/s10825-020-01606-

2.

[28] M. R. Islam, F. A. Mou, M. M. Rahman, and M. I. Hassan Bhuiyan, “Hollow core photonic crystal fiber for chemicals sensing in liquid analytes: Design and analysis,” *Int. J. Mod. Phys. B*, vol. 34, no. 28, pp. 1–13, 2020, doi: 10.1142/S0217979220502598.

[29] F. A. Mou, M. M. Rahman, A. Al Mahmud, M. R. Islam, and M. I. Hassan Bhuiyan, “Highly Sensitive Hollow Core Photonic Crystal Fiber Based Methyl-Alcohol Detector for Liquid Analytes in THz Regime,” *2020 IEEE Reg. 10 Symp. TENSYMP 2020*, no. June, pp. 1640–1643, 2020, doi: 10.1109/TENSYMP50017.2020.9230831.

[30] M. M. Rahman, F. A. Mou, M. I. H. Bhuiyan, and M. R. Islam, “Photonic crystal fiber based terahertz sensor for cholesterol detection in human blood and liquid foodstuffs,” *Sens. Bio-Sensing Res.*, vol. 29, p. 100356, 2020, doi: 10.1016/j.sbsr.2020.100356.

[31] M. A. Islam, M. R. Islam, Z. Tasnim, R. Islam, R. L. Khan, and E. Moazzam, “Low-Loss and Dispersion-Flattened Octagonal Porous Core PCF for Terahertz Transmission Applications,” *Iran. J. Sci. Technol. - Trans. Electr. Eng.*, vol. 44, no. 4, pp. 1583–1592, 2020, doi: 10.1007/s40998-020-00337-1.

[32] F. A. Mou, M. M. Rahman, M. R. Islam, and M. I. H. Bhuiyan, “Development of a photonic crystal fiber for THz wave guidance and environmental pollutants detection,” *Sens. Bio-Sensing Res.*, vol. 29, p. 100346, 2020, doi: 10.1016/j.sbsr.2020.100346.

[33] M. Moshiur Rahman, F. Akter Mou, M. Imamul Hassan Bhuiyan, and M. Rakibul Islam, “Design and characterization of a circular sectored core cladding structured photonic crystal fiber with ultra-low EML and flattened dispersion in the THz regime,” *Opt. Fiber Technol.*, vol. 55, no. January, p. 102158, 2020, doi: 10.1016/j.yofte.2020.102158.

[34] M. R. Islam, M. F. Kabir, K. M. A. Talha, and M. S. Islam, “A novel hollow core terahertz refractometric sensor,” *Sens. Bio-Sensing Res.*, vol. 25, no. July, p. 100295, 2019, doi: 10.1016/j.sbsr.2019.100295.

[35] M. M. Rahman, F. A. Mou, M. I. H. Bhuiyan, and M. R. Islam, “Extremely Low Effective Material Loss of Air Core Photonic Crystal Fiber for THz Guidance,” *Proc. 2019 IEEE Reg. 10 Symp. TENSYMP 2019*, vol. 7, pp. 716–720, 2019, doi: 10.1109/TENSYMP46218.2019.8971297.

[36] M. R. Islam, “Topas Based Low Loss and Dispersion Flatten Decagonal Porous Core

Photonic Crystal Fiber for Terahertz Communication," no. January, 2019.

[37] M. R. Islam, M. Arif Hossain, S. I. Ali, J. Sultana, and M. Saiful Islam, "Design and Characterization of an Ultra Low Loss, Dispersion-Flattened Slotted Photonic Crystal Fiber for Terahertz Application," *J. Opt. Commun.*, vol. 42, no. 4, pp. 619–626, 2021, doi: 10.1515/joc-2018-0152.

[38] M. S. Islam *et al.*, "Low loss and low dispersion hybrid core photonic crystal fiber for terahertz propagation," *Photonic Netw. Commun.*, vol. 35, no. 3, pp. 364–373, 2018, doi: 10.1007/s11107-017-0751-7.

[39] M. S. Islam, K. M. Samaun Reza, and M. R. Islam, "Topas based high birefringent and low loss single mode hybrid-core porous fiber for broadband application," *Indian J. Pure Appl. Phys.*, vol. 56, no. 5, pp. 399–404, 2018.

[40] M. S. Islam *et al.*, "Zeonex-based asymmetrical terahertz photonic crystal fiber for multichannel communication and polarization maintaining applications," *Appl. Opt.*, vol. 57, no. 4, p. 666, 2018, doi: 10.1364/ao.57.000666.

[41] J. Sultana, M. S. Islam, M. R. Islam, and D. Abbott, "High numerical aperture, highly birefringent novel photonic crystal fibre for medical imaging applications," *Electron. Lett.*, vol. 54, no. 2, pp. 61–62, 2018, doi: 10.1049/el.2017.3694.

[42] M. S. Islam *et al.*, "Extremely low material loss and dispersion flattened TOPAS based circular porous fiber for long distance terahertz wave transmission," *Opt. Fiber Technol.*, vol. 34, pp. 6–11, 2017, doi: 10.1016/j.yofte.2016.11.014.

[43] M. S. Islam, J. Sultana, J. Atai, D. Abbott, S. Rana, and M. R. Islam, "Ultra low-loss hybrid core porous fiber for broadband applications," *Appl. Opt.*, vol. 56, no. 4, p. 1232, 2017, doi: 10.1364/ao.56.001232.

[44] S. Rana *et al.*, "A highly birefringent slotted-core THz fiber," *Proc. 9th Int. Conf. Electr. Comput. Eng. ICECE 2016*, pp. 226–229, 2017, doi: 10.1109/ICECE.2016.7853897.

[45] S. Islam *et al.*, "Extremely low-loss, dispersion flattened porous-core photonic crystal fiber for terahertz regime," *Opt. Eng.*, vol. 55, no. 7, p. 076117, 2016, doi: 10.1117/1.oe.55.7.076117.

[46] M. R. Islam, A. Hossain, Z. Mustafa, and T. Tahsin, "A Novel Photonic Crystal Fiber Biosensor Using Single Hexagonal Lattice Structure," pp. 475–478, 2020.

[47] M. Rakibul, I. A. N. M. Iftekher, F. Noor, R. Hoque, and K. Taslim, “AZO - coated plasmonic PCF nanosensor for blood constituent detection in near - infrared and visible spectrum,” *Appl. Phys. A*, vol. 128, no. 1, pp. 1–13, 2022, doi: 10.1007/s00339-021-05220-2.

[48] M. R. Islam *et al.*, “Design and numerical analysis of a gold-coated photonic crystal fiber based refractive index sensor,” *Opt. Quantum Electron.*, vol. 53, no. 2, pp. 1–18, 2021, doi: 10.1007/s11082-021-02748-8.

[49] M. R. Islam *et al.*, “Surface plasmon resonance based highly sensitive gold coated PCF biosensor,” *Appl. Phys. A Mater. Sci. Process.*, vol. 127, no. 2, pp. 1–12, 2021, doi: 10.1007/s00339-020-04162-5.

[50] M. R. Islam *et al.*, “Design and Analysis of a Biochemical Sensor Based on Surface Plasmon Resonance with Ultra-high Sensitivity,” *Plasmonics*, vol. 16, no. 3, pp. 849–861, 2021, doi: 10.1007/s11468-020-01355-9.

[51] M. Rakibul Islam, M. M. I. Khan, F. Mehjabin, J. Alam Chowdhury, and M. Islam, “Design of a fabrication friendly & highly sensitive surface plasmon resonance-based photonic crystal fiber biosensor,” *Results Phys.*, vol. 19, no. August, p. 103501, 2020, doi: 10.1016/j.rinp.2020.103501.

[52] M. R. Islam, A. N. M. Iftekher, F. Noor, M. R. H. Khan, M. T. Reza, and M. M. Nishat, “AZO-coated plasmonic PCF nanosensor for blood constituent detection in near-infrared and visible spectrum,” *Appl. Phys. A Mater. Sci. Process.*, vol. 128, no. 1, pp. 1–13, 2022, doi: 10.1007/s00339-021-05220-2.

[53] M. R. Islam *et al.*, “Design of a dual spider-shaped surface plasmon resonance-based refractometric sensor with high amplitude sensitivity,” *IET Optoelectron.*, Feb. 2022, doi: 10.1049/OTE2.12084.

[54] M. R. Islam, E. Moazzam, R. Islam, and R. L. Khan, “Design and Investigation of a Low-Loss Surface Plasmon Resonance based Design and Investigation of a low-loss Surface Plasmon resonance based PCF biosensor with a gold coated structure,” no. August 2022, 2020, doi: 10.1109/ICECE51571.2020.9393045.

[55] M. Rakibul, I. Fahim, Y. Rakib, H. Antor, and M. Hassan, “An Eye - Shaped Ultra - Sensitive Localized Surface Plasmon Resonance – Based Biochemical Sensor,”

Plasmonics, no. 0123456789, 2021, doi: 10.1007/s11468-021-01501-x.

[56] M. R. Islam *et al.*, "Sensing and Bio-Sensing Research Trigonal cluster-based ultra-sensitive surface plasmon resonance sensor for multipurpose sensing," *Sens. Bio-Sensing Res.*, vol. 35, no. January, p. 100477, 2022, doi: 10.1016/j.sbsr.2022.100477.

[57] M. R. Islam *et al.*, "Design and analysis of a QC-SPR-PCF sensor for multipurpose sensing with supremely high FOM," *Appl. Nanosci.*, vol. 12, no. 1, pp. 29–45, 2022, doi: 10.1007/s13204-021-02150-6.

[58] M. Rakibul, I. Kazi, R. Hasan, M. Islam, A. Nayeem, and M. Iftekher, "Design of a Dual Cluster and Dual Array - Based PCF - SPR Biosensor with Ultra - high WS and FOM," *Plasmonics*, pp. 1171–1182, 2022, doi: 10.1007/s11468-022-01612-z.

[59] S. Bin Islam, K. R. Hasan, M. R. Islam, M. J. Nayen, and A. N. M. Iftekher, "Dual-polarized highly sensitive surface-plasmon-resonance-based chemical and biomolecular sensor," *Appl. Opt. Vol. 59, Issue 11, pp. 3296-3305*, vol. 59, no. 11, pp. 3296–3305, Apr. 2020, doi: 10.1364/AO.383352.

[60] M. R. Islam *et al.*, "Highly birefringent gold-coated SPR sensor with extremely enhanced amplitude and wavelength sensitivity," *Eur. Phys. J. Plus*, vol. 136, no. 2, pp. 1–14, 2021, doi: 10.1140/epjp/s13360-021-01220-6.

[61] M. R. Islam *et al.*, "Optik Design and analysis of birefringent SPR based PCF biosensor with ultra-high sensitivity and low loss," *Optik (Stuttg).*, vol. 221, no. May, p. 165311, 2020, doi: 10.1016/j.ijleo.2020.165311.

[62] M. Rahman, M. R. Islam, S. Siraz, and M. S. Anzum, "A high crosstalk modified D-shaped single-polarization filter for S and U for S and U band optical communication," *Opt. Quantum Electron.*, vol. 55, no. 3, pp. 1–14, 2023, doi: 10.1007/s11082-023-04542-0.

[63] M. Rakibul Islam, A. N. M. Iftekher, M. S. Anzum, M. Rahman, and S. Siraz, "LSPR Based Double Peak Double Plasmonic Layered Bent Core PCF-SPR Sensor for Ultra-Broadband Dual Peak Sensing," *IEEE Sens. J.*, vol. 22, no. 6, pp. 5628–5635, 2022, doi: 10.1109/JSEN.2022.3149715.

[64] V. S. Chaudhary and D. Kumar, "TOPAS based porous core photonic crystal fiber for terahertz chemical sensor," *Optik (Stuttg).*, vol. 223, no. June, p. 165562, 2020, doi:

10.1016/j.ijleo.2020.165562.

[65] S. Dash, V. Mathur, N. Pandey, and R. K. Sinha, “Terahertz Wave Propagation Characteristics in Graded Teflon Based Solid-Core Photonic Crystal Fibre,” *J. Phys. Conf. Ser.*, vol. 2426, no. 1, 2023, doi: 10.1088/1742-6596/2426/1/012021.

[66] M. Goto, A. Quema, H. Takahashi, S. Ono, and N. Sarukura, “Polarization-preserving teflon photonic crystal fiber waveguide for THz radiation,” *Conf. Dig. 2004 Jt. 29th Int. Conf. Infrared Millim. Waves 12th Int. Conf. Terahertz Electron.*, no. May 2014, pp. 139–140, 2004, doi: 10.1109/icimw.2004.1421992.

[67] N. Muduli, G. Palai, and S. K. Tripathy, “Realization of a beam splitter using a Photonic Crystal Fiber (PCF),” *Res. J. Phys. Appl. Sci.*, vol. 2, no. March, pp. 20–24, 2013.

[68] T. Parvin and K. Ahmed, “Design of Honeycomb Shaped Spectroscopy based Biosensor for the Detection of Tuberculosis Cells Design of Honeycomb Shaped Spectroscopy based Biosensor for”.

[69] G. J. Pearce, J. M. Pottage, D. M. Bird, P. J. Roberts, J. C. Knight, and P. S. J. Russell, “Hollow-core PCF for guidance in the mid to far infra-red,” *Opt. Express*, vol. 13, no. 18, p. 6937, 2005, doi: 10.1364/opex.13.006937.

[70] Y. Ni, Z. Lei, J. Shu, and P. Jiangde, “Dispersion of square solid-core photonic bandgap fibers,” *Opt. Express*, vol. 12, no. 13, p. 2825, 2004, doi: 10.1364/opex.12.002825.

[71] K. Ahmed and M. Morshed, “Design and numerical analysis of microstructured-core octagonal photonic crystal fiber for sensing applications,” *Sens. Bio-Sensing Res.*, vol. 7, pp. 1–6, 2016, doi: 10.1016/j.sbsr.2015.10.005.

[72] S. Li, “Equiangular spiral photonic crystal fiber for code synchronization in all-optical analog-to-digital conversion based on lumped time delay compensation scheme,” *Optik (Stuttg).*, vol. 127, no. 11, pp. 4693–4697, 2016, doi: 10.1016/j.ijleo.2016.02.017.

[73] Y. Ying *et al.*, “High Performance Dual-Core D-Shaped PCF Refractive Index Sensor Coated with Gold Grating,” *Photonics*, vol. 10, no. 4, 2023, doi: 10.3390/photonics10040473.

[74] S. E. E. Profile, “Hybrid Structure Hollow Core PCF using PBG Mechanism for the Application of Optical Fiber Under the Supervision of Hybrid Structure Hollow f Core PCF using PBG Mechanism for the Application of Optical Fiber Md . Enam Khan Under

the Supervision of Dr . Rus," no. January, 2021.

[75] J. Li, "A review : Development of novel fiber-optic platforms for bulk and surface refractive index sensing applications," *Sensors and Actuators Reports*, vol. 2, no. 1, p. 100018, 2020, doi: 10.1016/j.snr.2020.100018.

[76] J. K. Sahota, N. Gupta, and D. Dhawan, "Fiber Bragg grating sensors for monitoring of physical parameters : a comprehensive review," vol. 59, no. May, pp. 1–35, 2023, doi: 10.1117/1.OE.59.6.060901.

[77] R. C. Jorgenson and S. S. Yee, "A fiber-optic chemical sensor based on surface plasmon resonance," *Sensors Actuators B. Chem.*, vol. 12, no. 3, pp. 213–220, 1993, doi: 10.1016/0925-4005(93)80021-3.

[78] B. Liedberg, C. Nylander, and I. Lunström, "Surface plasmon resonance for gas detection and biosensing," *Sensors and Actuators*, vol. 4, no. C, pp. 299–304, 1983, doi: 10.1016/0250-6874(83)85036-7.

[79] C. E. H. Berger and J. Greve, "Differential SPR immunosensing," *Sensors Actuators, B Chem.*, vol. 63, no. 1, pp. 103–108, 2000, doi: 10.1016/S0925-4005(00)00307-5.

[80] D. Irawan, K. Ramadhan, and A. Azhar, "Design of PCF-SPR for Early Detection of Skin Cancer Infected Cells," *J. Penelit. Pendidik. IPA*, vol. 8, no. 5, pp. 2293–2298, 2022, doi: 10.29303/jppipa.v8i5.2120.

[81] V. Koubová *et al.*, "Detection of foodborne pathogens using surface plasmon resonance biosensors," *Sensors Actuators, B Chem.*, vol. 74, no. 1–3, pp. 100–105, 2001, doi: 10.1016/S0925-4005(00)00717-6.

[82] J. Homola, "Surface plasmon resonance sensors for detection of chemical and biological species," *Chem. Rev.*, vol. 108, no. 2, pp. 462–493, 2008, doi: 10.1021/cr068107d.

[83] M. Mohseni-Dargah, Z. Falahati, B. Dabirmanesh, P. Nasrollahi, and K. Khajeh, "Machine learning in surface plasmon resonance for environmental monitoring," *Artif. Intell. Data Sci. Environ. Sens.*, pp. 269–298, Jan. 2022, doi: 10.1016/B978-0-323-90508-4.00012-5.

[84] K. A. Rikta, M. S. Anower, M. S. Rahman, and M. M. Rahman, "SPR biosensor using SnSe-phosphorene heterostructure," *Sens. Bio-Sensing Res.*, vol. 33, p. 100442, Aug. 2021, doi: 10.1016/J.SBSR.2021.100442.

[85] P. S. Pandey, S. K. Raghuwanshi, A. Shadab, M. T. I. Ansari, U. K. Tiwari, and S. Kumar, "SPR Based Biosensing Chip for COVID-19 Diagnosis - A Review," *IEEE Sens. J.*, vol. 22, no. 14, pp. 13800–13810, 2022, doi: 10.1109/JSEN.2022.3181423.

[86] C. Zhou, "Localized surface plasmonic resonance study of silver nanocubes for photonic crystal fiber sensor," *Opt. Lasers Eng.*, vol. 50, no. 11, pp. 1592–1595, 2012, doi: 10.1016/j.optlaseng.2012.05.020.

[87] P. S. S. Dos Santos, J. M. M. M. de Almeida, and L. C. C. Coelho, "Study of LSPR Spectral Analysis Techniques on SPR Optical Fiber Sensors," *U.Porto J. Eng.*, vol. 8, no. 3 Special Issue, pp. 12–17, 2022, doi: 10.24840/2183-6493_008.003_0004.

[88] M. R. Islam, A. N. M. Iftekher, I. Marshad, N. F. Rity, and R. U. Ahmad, "Analysis of a dual peak dual plasmonic layered LSPR-PCF sensor – Double peak shift sensitivity approach," *Optik (Stuttg).*, vol. 280, p. 170793, Jun. 2023, doi: 10.1016/J.IJLEO.2023.170793.

[89] M. Proenca, M. Rodrigues, F. Vaz, and J. Borges, "Carbon Monoxide (CO) Sensor Based on Au Nanoparticles Embedded in a CuO Matrix by HR-LSPR Spectroscopy at Room Temperature," *IEEE Sensors Lett.*, vol. 5, no. 5, 2021, doi: 10.1109/LSENS.2021.3074603.

[90] "Development of LSPR-based optical biosensors for the label-free detection of biomolecular interactions in high-density peptide arrays." https://www.researchgate.net/publication/280663098_Development_of_LSPR-based_optical_biosensors_for_the_label-free_detection_of_biomolecular_interactions_in_high-density_peptide_arrays (accessed May 27, 2023).

[91] T. Tang *et al.*, "Promoting Plasmonic Hot Hole Extraction and Photothermal Effect for the Oxygen Evolution Reactions," *Chemistry*, 2023, doi: 10.1002/CHEM.202300225.

[92] M. Hautakorpi, M. Mattinen, and H. Ludvigsen, "Surface-plasmon-resonance sensor based on suspended-core microstructured optical fiber," *2008 Jt. Conf. Opto-Electronics Commun. Conf. Aust. Conf. Opt. Fibre Technol. OECC/ACOFT 2008*, vol. 16, no. 12, pp. 2390–2392, 2008, doi: 10.1109/OECCACOFT.2008.4610571.

[93] Y. E. Monfared and M. Qasymeh, "Plasmonic Biosensor for Low - Index Liquid Analyte

Detection Using Graphene - Assisted Photonic Crystal Fiber," *Plasmonics*, pp. 881–889, 2021, doi: 10.1007/s11468-020-01308-2.

[94] N. Luan, R. Wang, W. Lv, and J. Yao, "Surface plasmon resonance sensor based on D-shaped microstructured optical fiber with hollow core," *Opt. Express*, vol. 23, no. 7, p. 8576, 2015, doi: 10.1364/oe.23.008576.

[95] H. S. Sehmi, W. Langbein, and E. A. Muljarov, "Optimizing the Drude-Lorentz model for material permittivity: Method, program, and examples for gold, silver, and copper," *Phys. Rev. B*, vol. 95, no. 11, p. 115444, Mar. 2017, doi: 10.1103/PHYSREVB.95.115444/FIGURES/9/MEDIUM.

[96] "(2) Optics hecht and zajac 4th ed | Filipe Santos - Academia.edu."

[97] M. S. Islam *et al.*, "A Hi-Bi Ultra-Sensitive Surface Plasmon Resonance Fiber Sensor," *IEEE Access*, vol. 7, no. i, pp. 79085–79094, 2019, doi: 10.1109/ACCESS.2019.2922663.

[98] V. Kaur and S. Singh, "Design approach of solid-core photonic crystal fiber sensor with sensing ring for blood component detection," *J. Nanophotonics*, vol. 13, no. 02, p. 1, 2019, doi: 10.1117/1.jnp.13.026011.

[99] A. A. Rifat, G. Amouzad Mahdiraji, D. M. Chow, Y. G. Shee, R. Ahmed, and F. R. M. Adikan, "Photonic crystal fiber-based surface plasmon resonance sensor with selective analyte channels and graphene-silver deposited core," *Sensors (Switzerland)*, vol. 15, no. 5, pp. 11499–11510, 2015, doi: 10.3390/s150511499.

[100] P. R. West, S. Ishii, G. Naik, N. Emani, V. M. Shalaev, and A. Boltasseva, "<Shalev_Review-Plasmon.Pdf>," pp. 1–28.

[101] F. Haider, R. A. Aoni, R. Ahmed, M. S. Islam, and A. E. Miroshnichenko, "Propagation Controlled Photonic Crystal Fiber-Based Plasmonic Sensor via Scaled-Down Approach," *IEEE Sens. J.*, vol. 19, no. 3, pp. 962–969, 2019, doi: 10.1109/JSEN.2018.2880161.

[102] M. Rakibul Islam, A. N. M. Iftekher, M. S. Anzum, M. Rahman, and S. Siraz, "LSPR Based Double Peak Double Plasmonic Layered Bent Core PCF-SPR Sensor for Ultra-Broadband Dual Peak Sensing," *IEEE Sens. J.*, vol. 22, no. 6, pp. 5628–5635, Mar. 2022, doi: 10.1109/JSEN.2022.3149715.

[103] M. R. Hasan *et al.*, “Spiral photonic crystal fiber-based dual-polarized surface plasmon resonance biosensor,” *IEEE Sens. J.*, vol. 18, no. 1, pp. 133–140, 2018, doi: 10.1109/JSEN.2017.2769720.

[104] A. Kumar Paul, A. Krishno Sarkar, A. B. S. Rahman, and A. Khaleque, “Twin core photonic crystal fiber plasmonic refractive index sensor,” *IEEE Sens. J.*, vol. 18, no. 14, pp. 5761–5769, 2018, doi: 10.1109/JSEN.2018.2841035.

[105] S. Chakma, M. A. Khalek, B. K. Paul, K. Ahmed, M. R. Hasan, and A. N. Bahar, “Gold-coated photonic crystal fiber biosensor based on surface plasmon resonance: Design and analysis,” *Sens. Bio-Sensing Res.*, vol. 18, pp. 7–12, 2018, doi: 10.1016/j.sbsr.2018.02.003.

[106] S. Chu *et al.*, “Influence of the Sub-peak of Secondary Surface Plasmon Resonance onto the Sensing Performance of a D-shaped Photonic Crystal Fibre Sensor,” *IEEE Sens. J.*, vol. PP, no. c, p. 1, 2019, doi: 10.1109/JSEN.2019.2953393.

[107] S. Jain, K. Choudhary, and S. Kumar, “Photonic crystal fiber-based SPR sensor for broad range of refractive index sensing applications,” *Opt. Fiber Technol.*, vol. 73, p. 103030, Oct. 2022, doi: 10.1016/J.YOFTE.2022.103030.

[108] J. N. Dash, R. Das, and R. Jha, “AZO coated microchannel incorporated PCF-based SPR sensor: A numerical analysis,” *IEEE Photonics Technol. Lett.*, vol. 30, no. 11, pp. 1032–1035, 2018, doi: 10.1109/LPT.2018.2829920.

[109] P. Chu, J. Chen, Z. Xiong, and Z. Yi, “Controllable frequency conversion in the coupled time-modulated cavities with phase delay,” *Opt. Commun.*, vol. 476, p. 126338, 2020, doi: 10.1016/j.optcom.2020.126338.

[110] P. J. A. Sazio *et al.*, “Microstructured optical fibers as high-pressure microfluidic reactors,” *Science (80-.).*, vol. 311, no. 5767, pp. 1583–1586, 2006, doi: 10.1126/science.1124281.

[111] D. K. Kim *et al.*, “Label-free DNA biosensor based on localized surface plasmon resonance coupled with interferometry,” *Anal. Chem.*, vol. 79, no. 5, pp. 1855–1864, 2007, doi: 10.1021/ac061909o.

[112] C. D. Mathers and D. Loncar, “Projections of global mortality and burden of disease from 2002 to 2030,” *PLoS Med.*, vol. 3, no. 11, pp. 2011–2030, 2006, doi:

10.1371/journal.pmed.0030442.

[113] T. J. Park, S. J. Lee, D. K. Kim, N. S. Heo, J. Y. Park, and S. Y. Lee, “Development of label-free optical diagnosis for sensitive detection of influenza virus with genetically engineered fusion protein,” *Talanta*, vol. 89, pp. 246–252, 2012, doi: 10.1016/j.talanta.2011.12.021.

[114] J. H. Lee, B. C. Kim, B. K. Oh, and J. W. Choi, “Highly sensitive localized surface plasmon resonance immunosensor for label-free detection of HIV-1,” *Nanomedicine Nanotechnology, Biol. Med.*, vol. 9, no. 7, pp. 1018–1026, 2013, doi: 10.1016/j.nano.2013.03.005.

[115] T. Ohta, M. Ito, T. Kotani, and T. Hattori, “Emission enhancement of laser-induced breakdown spectroscopy by localized surface plasmon resonance for analyzing plant nutrients,” *Appl. Spectrosc.*, vol. 63, no. 5, pp. 555–558, 2009, doi: 10.1366/000370209788346896.

[116] T. J. Lin, K. T. Huang, and C. Y. Liu, “Determination of organophosphorous pesticides by a novel biosensor based on localized surface plasmon resonance,” *Biosens. Bioelectron.*, vol. 22, no. 4 SPEC. ISS., pp. 513–518, 2006, doi: 10.1016/j.bios.2006.05.007.

[117] K. Takemura, “Surface plasmon resonance (Spr)-and localized spr (lspr)-based virus sensing systems: Optical vibration of nano-and micro-metallic materials for the development of next-generation virus detection technology,” *Biosensors*, vol. 11, no. 8, 2021, doi: 10.3390/bios11080250.

[118] D. L. Zhong, F. L. Yuan, L. Lian, and Z. H. Cheng, “A localized surface plasmon resonance light-scattering assay of mercury (II) on the basis of Hg2+-DNA complex induced aggregation of gold nanoparticles,” *Environ. Sci. Technol.*, vol. 43, no. 13, pp. 5022–5027, 2009, doi: 10.1021/es9001983.